ARTICLES

Femtosecond Real-Time Probing of Reactions. 23. Studies of Temporal, Velocity, Angular, and State Dynamics from Transition States to Final Products by Femtosecond-Resolved Mass Spectrometry

Dongping Zhong and Ahmed H. Zewail*

Arthur Amos Noyes Laboratory of Chemical Physics, California Institute of Technology, Pasadena, California 91125

Received: December 15, 1997; In Final Form: January 26, 1998

In this contribution, we give a full account of the approach of femtosecond, time-resolved mass spectrometry in molecular beams for the studies of the elementary steps of complex reactions and the application to different systems. The level of complexity varies from diatomics to polyatomics, from direct-mode to complex-mode, from one-center, to two-center, to four-center, and from uni- to bimolecular reactions. The systems studied are iodine, cyanogen iodide, methyl iodide, iodobenzene, 1,2-diiodotetrafluoroethane, mercury iodide, benzene·iodine complexes, and methyl iodide dimers. By resolving the *femtosecond dynamics* and simultaneously observing the evolution of *velocity*, *angular*, and *state* distribution(s) of the reaction, we are able to study multiple reaction paths, the nature of transition-state geometry and dynamics, coherent wave-packet motion, evolution of energy disposal, and the nonconcerted motion in multicenter reactions. These phenomena and concepts are elucidated in dissociation, elimination, and charge-transfer reactions and in the inelastic and reactive pathways of bimolecular reactions. Theoretical phenomenology, using frontier orbitals and molecular dynamics, are invoked to provide a relationship between the observed dynamics and molecular structures.

I. Introduction

Over the past two decades, a variety of detection techniques has been used to probe the ultrafast dynamics of chemical reactions (for recent books see refs 1−5). These include the use of absorption, laser-induced fluorescence (LIF), multiphoton ionization (MPI), photoelectron spectroscopy, nonlinear degenerate four-wave mixing, stimulated emission pumping, Coulomb explosion, and time-resolved mass spectrometry in molecular beams. One of the techniques used extensively in this laboratory is mass spectrometry with femtosecond (fs), and earlier with picosecond (ps), resolution.

The advantages of femtosecond-resolved mass spectrometry are numerous (see refs 1−7). First, the mass resolution identifies reaction constituents. Second, as reported from this laboratory,[8] the kinetic-energy distribution(s) can be followed as a function of time, allowing us to map changes in velocities of fragments. Third, by invoking polarized femtosecond pulses relative to the time-of-flight axis, one is able to study the angular distributions and the nature of the transition(s) involved. Finally, the state of the final fragment could be resolved by selective ionization with the probe femtosecond pulse, using, for example, resonance-enhanced MPI or REMPI. Thus, for a given velocity or velocity range we can monitor the temporal evolution of the reaction.

With these capabilities of *temporal*, *velocity*, *angular*, and *state* resolution of the dynamics, it is possible to study a variety of reactions (for a review see ref 9), elementary and complex. In this paper, we give a full account of the approach with applications to many reactions. The level of complexity varies from diatomics to polyatomics, from direct-mode to complex-mode, and from one-center to two-center to four-center reactions. The reactions reported here are uni- and bimolecular in nature and are those of iodine, cyanogen iodide, methyl iodide, iodobenzene, 1,2-diiodotetrafluoroethane, mercury iodide, benzene·iodine complexes, and methyl iodide dimers. We systematically study the dynamics in these systems from results of (i) the femtosecond temporal dynamics, (ii) the time- and kinetic-energy-resolved time-of-flight (KETOF) mass spectra, (iii) the angle-resolved KETOF distributions, and (iv) the state-resolved (I and I*) dynamics.

The paper is outlined as follows. In section II, the experimental techniques are described, including the experimental apparatus and the KETOF method. In section III, a methodology is presented for detecting simultaneously the transition-state species and final products using only one femtosecond pulse. The experimental results and discussion for eight different systems are given in section IV. Finally, we give our conclusion in sectionV.

II. Experimental Techniques

A. Experimental Apparatus and Mass Spectra. All experiments were performed in a two-chamber molecular-beam apparatus integrated with a tunable femtosecond laser system, and both are schematically shown in Figures 1 and 2. Most details have been described in a recent publication,[8b] and only a summary is given here.

The femtosecond oscillator generates pulses typically with ∼200 fs full width at half-maximum (fwhm) and 1−2 nJ energy

S1089-5639(98)00519-2 CCC: $15.00
Published on Web 03/21/1998

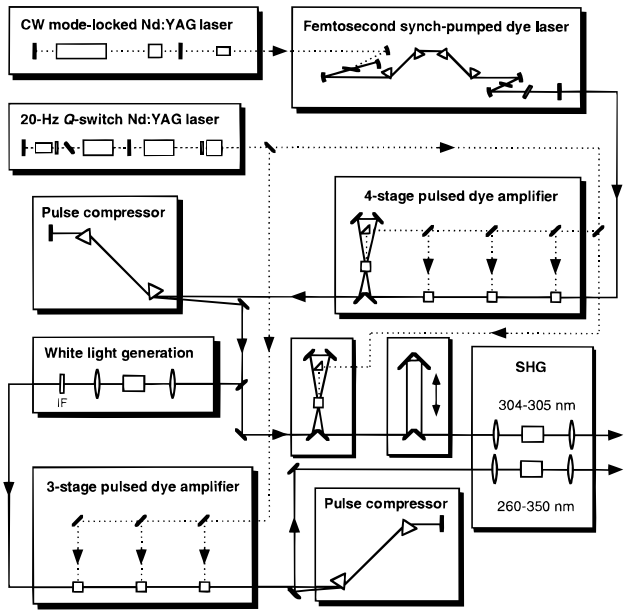

Figure 1. Schematic description of the femtosecond laser system. Note that two tunable femtosecond pulses were utilized and in synchrony. See the text for details.

per pulse. The pulse wavelength was tuned to be centered at ~609 nm. These femtosecond pulses were then passed through a home-built four-stage pulsed dye amplifier to reach an energy of 300−400 μJ/pulse. The amplified pulses were compressed through an SF-10 prism pair to compensate for the group-velocity dispersion in the amplification process. To generate 277-nm pump pulses, 80% of the beam was split off by a beam splitter and was focused into a small quartz cell containing D_2O solution to generate a white-light continuum. An interference filter was used to select a different portion of the continuum at the desired wavelength. This portion was then reamplified through a three-stage pulsed dye amplifier. The resulting pulses were recompressed by another SF-10 prism pair and then frequency-doubled through a 0.5-mm KDP nonlinear crystal to produce the pump beam (277 nm and ~10 μJ/pulse).

Only for the I_2 system was the pump wavelength at 690 nm for the A-state excitation. The remaining 20% of the 609-nm laser beam was sent to a double-passed single-stage dye amplifier and then delayed in time by a retroreflector mounted on a computer-controlled translation stage. A 0.5-mm KDP crystal was used for frequency doubling to obtain the probe beam at around 304.5 nm (~20 μJ/pulse) for 2 + 1 REMPI detection of free iodine atoms. Finally, the pump and probe pulses were recombined collinearly by a dichroic beam splitter and were focused and spatially overlapped in the extraction region of the TOF mass spectrometer.

A supersonic molecular beam containing the species of interest was generated in the first chamber, skimmed, and intersected by the femtosecond laser beams in the extraction region of a two-stage linear TOF-MS housed in the second chamber. A pair of deflection plates was employed in the field-free region to correct for the drift of ion trajectories due to the molecular-beam velocity component perpendicular to the TOF axis (z). The ions were collected by a 25-mm-diameter microchannel plate assembly (MCP). The molecular beam, TOF-MS axis, and the femtosecond laser beams were orthogonal to one another. For most results reported here, the pump laser polarization was parallel to the TOF-MS axis and orthogonal to the probe laser polarization. In some magic-angle experiments, the pump laser polarization was rotated at an angle of 54.7° with respect to the TOF-MS axis by a half-wave plate prior to the frequency doubling. The TOF-MS was also used as a kinetic-energy spectrometer, as described in section II.B, to resolve the translational-energy distribution of reaction products.

Time-resolved transients were obtained by monitoring the ion signal of a certain mass channel using a boxcar integrator while the pump−probe delay time was scanned. The free iodine atoms produced in reactions were detected through the 2 + 1 REMPI scheme; the I^+ intensity is very sensitive to the probe wavelength. By adjustment of a birefringent filter placed in the femtosecond oscillator, the probe wavelength was carefully tuned and was measured by a calibrated monochromator. The bandwidth was fixed within ~2 nm and covered several two-photon-allowed atomic transitions of the ground state $^2P_{3/2}$ (I, 304.67, 304.55, and 303.69 nm) and the spin−orbit excited state $^2P_{1/2}$ (I*, 305.57 and 304.02 nm). Therefore, the probe pulses simultaneously detected both I and I* atoms with about equal efficiency.

The zero-of-time and the cross correlation of the pump and probe pulses were determined by measuring the transient rise of the aniline or *N*,*N*-diethylaniline REMPI signal through their S_1 states immediately after the experiments were done in the molecular beam. Since the S_1 state is long-lived, the transient rise is equivalent to the convolution of the pump−probe correlation with a step function on the time scales of interest. The typical pump−probe cross correlation was 450 ± 50 fs fwhm. Although a much shorter probe pulse can be easily reached, the resulting broader spectrum leads to a huge I^+ background in most molecules and a loss of tunability for the iodine REMPI detection. All transients reported here result from one-photon excitation as checked by the power dependence of the observed signal.

Molecules of interest were seeded in ~800 Torr of He and were expanded through the pulsed valve. The mixture was made by flowing the He over the sample far away from the nozzle. To avoid cluster formation in the expansion, the monomer condition was carefully controlled in two ways: the leading edge of the gas pulse was sampled by varying the delay time between the femtosecond laser pulses and the pulsed valve opening, and the low vapor pressure of samples was used by maintaining the samples at low temperatures.

All samples were purchased from Aldrich except CF_2I-CF_2I, which was obtained from PCR. The iodine (I_2, 99.999% pure) was used at room temperature (vapor pressure of ~1 Torr). ICN (93%) was further purified through recrystallization followed by vacuum distillation and used at room temperature (~1 Torr of vapor). Methyl iodide (CH_3I, 99.5%) was cooled to −50 °C, giving a ~7−8 Torr of vapor. $C_2F_4I_2$ (≥97%), without further purification, was maintained at −35 °C with a vapor pressure less than 10 Torr. Both mercury iodide (HgI_2, ~99.999%) and iodobenzene (IBz, ≥98%) were heated to 130 and 70 °C, providing vapor pressures less than 1 and ~20 Torr, respectively. Benzene (Bz) was cooled to −45 °C, giving ~0.5 Torr of vapor pressure, and was then mixed with 1 Torr of I_2 before expansion. The TOF mass spectra are shown in Figure 3. The natural-isotope distribution of Hg (196−204) is also presented by the parent HgI_2 mass peak in the inset of Figure 3b. In contrast to the nanosecond laser experiments, where many parent ions were not observed, most parent ions here are major mass peaks in the TOF mass spectra. Note that no dimer traces were found in parts a and b of Figure 3, and the fragment mass is mostly due to ion fragmentation. For the bimolecular

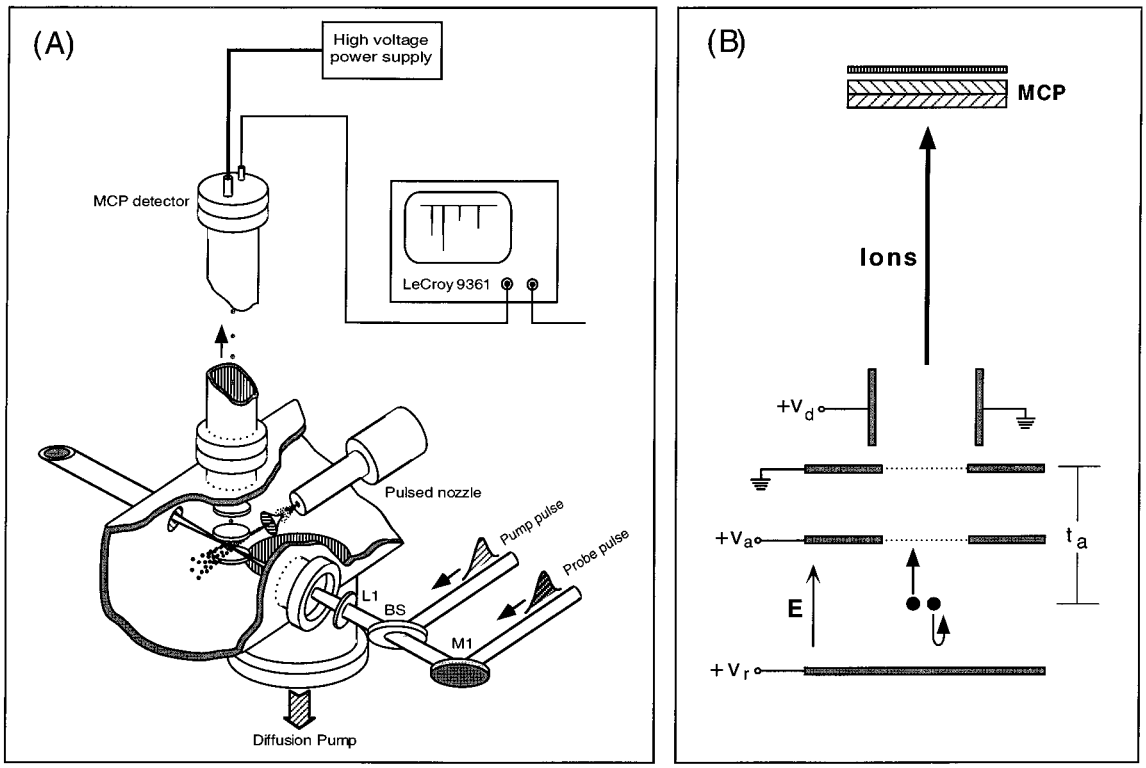

Figure 2. (A) Schematic representation of the molecular-beam apparatus integrated with two femtosecond laser beams. The pulsed nozzle and the TOF-MS are located in two separate chambers connected by a skimmer. (B) Diagram showing the "turnaround time" for two ions initially moving parallel to the TOF-MS axis with the same speed but in opposite directions. The time (t_a), which the ion spends in the acceleration region, is about several microseconds in our TOF arrangement.

reactions in Figure 3c, the gas-mixing conditions are well controlled to eliminate larger clusters, except the 1:1 complexes.

The arrival time of ions from the ionization zone to the detector is in the microsecond range, and this time depends on the ion mass, the applied acceleration electric field (E), and the flight distance. Usually, the time (t_a) the ions spend in the acceleration region is about several microseconds under the conditions used in this laboratory (see Figure 2B). When ion fragmentation ($AB^{+}* \rightarrow A^{+} + B$) occurs in the different regions during the flight, the ion fragment (A^{+}) will appear at different positions in the mass spectra. We consider three different cases.

If the molecule AB is ionized at $t = 0$ and then excited AB^{+} fragments on the femtosecond-to-picosecond time scale, that is, fragmentation occurs in the ionization zone, then the mass signal is well defined and the mass peaks of A^{+} and AB^{+} are clearly separated at the normal positions. When the ion has a long lifetime in the microsecond range, that is, fragmentation starts after the ion flies out of the acceleration region, A^{+} will appear at the same TOF (i.e., mass) as the parent ion AB^{+} because the times that ions spend in the field-free region only depend on the initial velocity, not the mass. If the ion breaks in the acceleration region ($\sim$1 μs), the A^{+} signal would appear at the normal position but will have a tail toward AB^{+} at longer arrival times of A^{+}, as observed in the benzene-cation fragmentation.[10] However, independent of how long the lifetime of $AB^{+}*$ is, the transient of the fragment A^{+} for femtosecond pump−probe experiments should be the same as that of AB^{+} because both transients reflect the dynamics of the neutral transition-state $AB^{*‡}$ species.

B. KETOF Method. To measure the translational-energy distributions released from the dissociation and the temporal behavior of transition states, we have used the REMPI detection in combination with femtosecond techniques and a kinetic-energy-resolved TOF-MS, namely, fs−KETOF, and applied it to several typical cases.[8,11−14] The KETOF technique, without time resolution, has been used by many groups,[15−19] and it is a mass-spectrometric version of Doppler photofragment spectroscopy.[20] In the following, we will briefly describe the basic idea and then describe two different methods used in our studies.

The velocity distribution due to fragmentation causes a spread around the central time-of-flight T_0. The spread in time ΔT is usually called "turn-around time" and is a linear function of the velocity projection onto the TOF axis v_z, which can be shown to be

$$\Delta T = \frac{2m|v_z|}{qE} \tag{1}$$

where m and q are the mass and charge of the ionized fragment and E is the extraction electric-field strength, as schematically shown in Figure 2B. By observing the KETOF distribution together with the well-defined excitation polarization, we can transform the v_z distribution to the speed and spatial distributions of the fragment. Two useful methods, by use of the magic angle[21−23] and the discrimination aperture,[16,24] are described in the following for the different cases under study.

When a molecule is dissociated through a one-photon excitation by linearly polarized light, the velocity distribution of a fragment can be written as the product of two functions: $f(v)$, the speed distribution, and $I(\theta)$, the angular distribution. The speed distribution is determined by the energetics of the dissociation. The angular distribution is axially symmetric with respect to the electric vector $\hat{\epsilon}$ of the light and has the form[25]

$$I(\theta) = \frac{1}{4\pi}[1 + \beta P_2(\cos\theta)] \tag{2}$$

where θ is the angle between the final recoil direction and $\hat{\epsilon}_{pu}$,

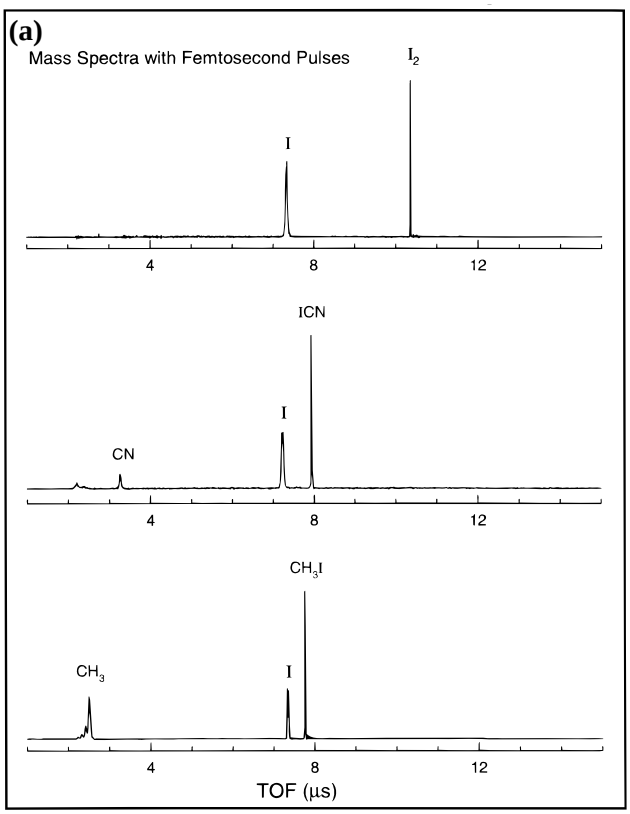

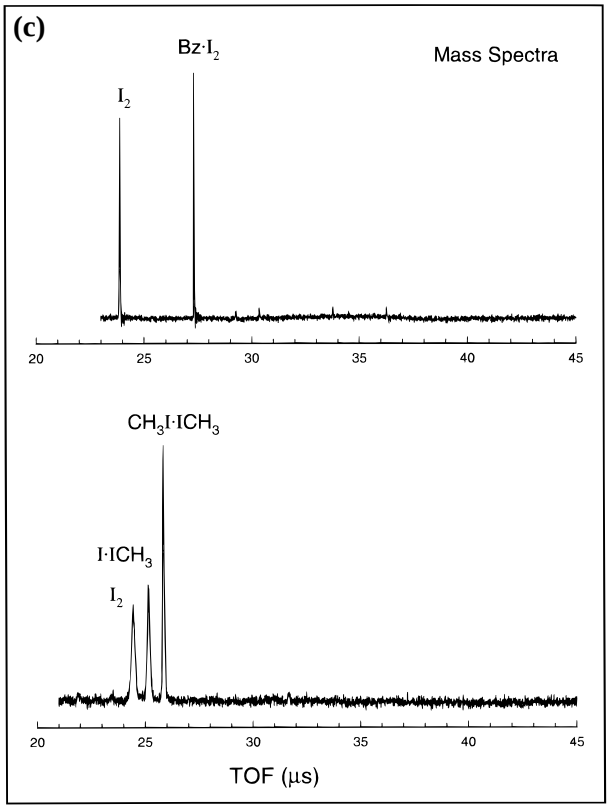

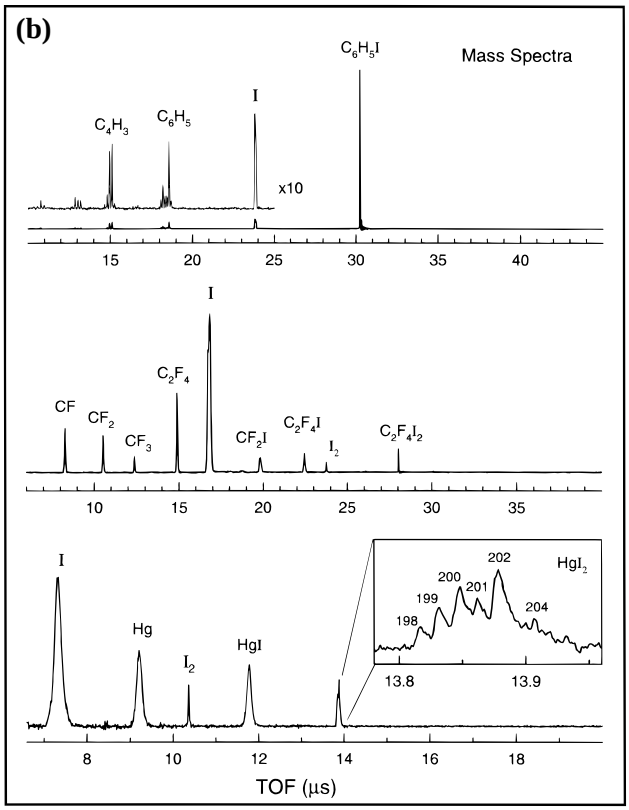

Figure 3. (a) TOF mass spectra obtained from the expansion of a mixture of 700 Torr of He with I_2 (1 Torr), ICN (~1 Torr), and CH_3I (~7 Torr) under the *monomer* condition. Both pump and probe pulses were used, and the delay time was 6 ps. Note that parent peaks are dominant, in contrast to results of nanosecond experiments (see text). (b) TOF mass spectra obtained from the expansion of a mixture of 700 Torr He with C_6H_5I (~20 Torr), $C_2F_4I_2$ (~10 Torr), and HgI_2 (1 Torr) under the *monomer* condition. Both pump and probe pulses were employed and the delay time was fixed at 100 ps. The broad peaks of Hg, HgI, and HgI_2 are due to the isotope distribution of Hg (196−204 amu), which is shown in the inset. (c) TOF mass spectra obtained from the expansion of a mixture of 0.5 Torr of benzene with 1 Torr of iodine in He (700 Torr). For generating the methyl iodide dimer, a mixture of 7 Torr of CH_3I with 700 Torr of He was used. Time delay between the femtosecond laser pulses and the pulsed valve opening was carefully varied. Note that no larger cluster traces were found except the binary complexes.

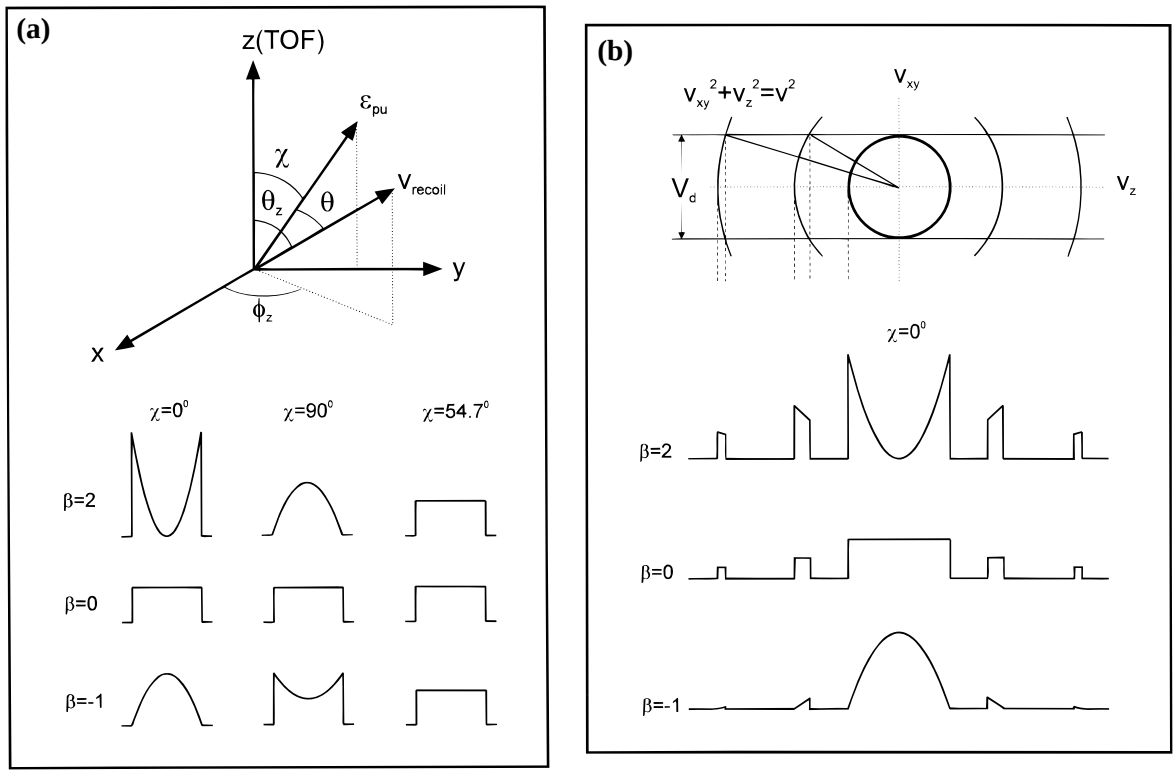

Figure 4. (a) Coordinate system used in describing the fragment angular-velocity distribution in the KETOF experiment. $\hat{\epsilon}_{pu}$ is the electric vector of the femtosecond pump laser pulse, which was kept in the *yz* plane. V_{recoil} is the fragment recoil direction. The lower part shows the theoretical predictions of the v_z distributions for some representative β's and χ's for single-speed fragments. Note that the distributions for $\beta = 0$ and $\chi = 54.7°$ are identical. (b) Two-dimensional (v_z, v_{xy}) depiction of the v_{xy} discrimination for three recoil speeds given by the circles. The discrimination velocity v_d, which discriminates against photoions with $v_{xy} \geq v_d$, is also shown. The lower part gives the simulated recoil velocity distributions of the single-speed fragment in the v_z domain without and with the v_{xy} discrimination for $\chi = 0°$ and three typical β's. The higher the recoil speed, the stronger the v_{xy} discrimination.[16,24]

as shown in Figure 4a. β is the recoil anisotropy parameter and $P_2(\cos\theta)$ is the second Legendre polynomial. The β parameter is determined, in the classic picture, by the direction of the transition dipole relative to the recoil velocity of the parent molecule and by the time scale of the dissociation. Its values can range from 2 to -1, corresponding to a range from purely *parallel* to *perpendicular* transitions, respectively.

In our experiments, the $\hat{\epsilon}_{pu}$ direction is kept in the *yz* plane. By use of the relations of $v_z = v\cos\theta_z$ and $\cos\theta = \cos\theta_z \cos\chi + \sin\theta_z \sin\chi \sin\varphi_z$, the v_z distribution can be expressed as

$$f(v_z, \chi) = \int_{|v_z|}^{\infty} \frac{1}{2v}\left[1 + \beta(v)P_2(\cos\chi)P_2\left(\frac{v_z}{v}\right)\right] f(v)v^2\,\mathrm{d}v \quad (3)$$

where χ is the angle between the *z* axis and the pump laser polarization $\hat{\epsilon}_{pu}$. Of particular importance is the special case of $\chi = 54.7°$, or the "magic angle", where $P_2(\cos\chi) = 0$. Therefore, the distribution is independent of β and becomes

$$f(v_z, 54.7°) = \int_{|v_z|}^{\infty} \frac{1}{2v} f(v)v^2\,\mathrm{d}v \quad (4)$$

At this pump angle, the v_z profile depends only on the scalar speed distribution. Equation 4 allows the speed distribution to be extracted directly by differentiation:

$$f(v) = -\frac{2}{v}\frac{\mathrm{d}}{\mathrm{d}v_z} f(v_z, 54.7°)|_{v_z=v} \quad (5)$$

The speed probability distribution and the fragment translational-energy distribution can be obtained:

$$g(v) = v^2 f(v) \quad (6a)$$

$$P(E_T) = \frac{g(v)}{mv} \quad (6b)$$

Once $f(v)$ is known, the anisotropy parameter $\beta(v)$ can also be derived by fitting the v_z distribution measured at the parallel polarization ($\chi = 0°$) according to eq 3. We have used this method to study I_2, ICN, CH_3I, $C_2F_4I_2$, HgI_2, $Bz{\cdot}I_2$, and $CH_3I{\cdot}CH_3I$ molecules and resolved the *state, velocity, and angular* time evolution of products.

Instead of using the differentiation method to obtain $f(v)$ and the numerical fitting for $\beta(v)$, another approach, which is approximate, may be used, and it is often used. It involves measuring the fs−KETOF distribution by employing a discrimination aperture (or namely, the core-sampling condition). Experimentally, a small aperture was placed just before the MCP detector to discriminate against collecting the ions that have v_{xy} components larger than the discrimination value v_d, as illustrated in Figure 4b. The method has been recently detailed by two other groups,[16,24] and here, only relevant points to our experiments are described.

When the molecular dissociation results in two velocity distributions, such as high- and low-velocity components, we are especially able to completely separate the two distributions in this one-dimensional v_z profile. For the high-velocity component, the signal only in the small solid angle ($0 \leq \theta \leq \arcsin(v_d/v)$) is collected and the KETOF distribution appears only in the larger v_z region and truncates between v and $(v^2 - v_d^2)^{1/2}$ and between $-v$ and $-(v^2 - v_d^2)^{1/2}$. However, for the low-velocity distribution, all ions are detected if the maximum

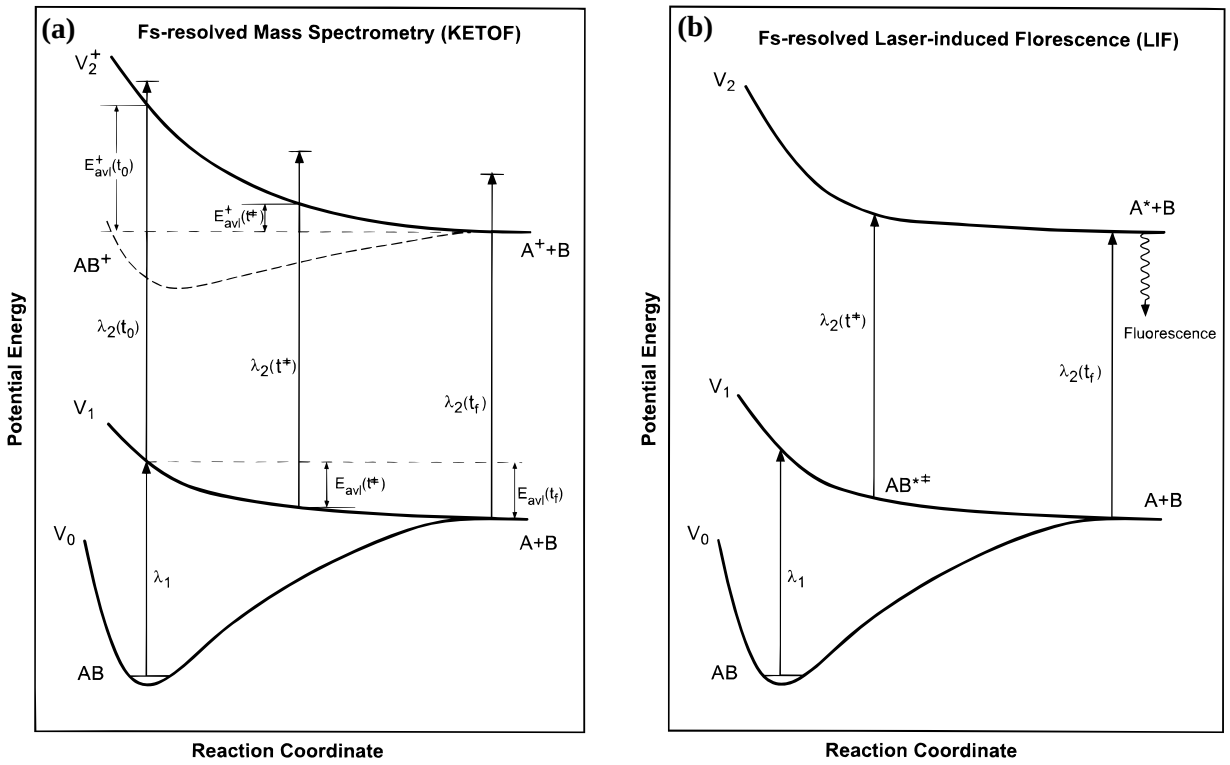

Figure 5. (a) General REMPI/MPI scheme for probing simultaneously transition-state species and final products using only one probe femtosecond pulse. V_0 and V_1 are the neutral ground- and excited-state PESs of the molecule AB, respectively. At time $t = 0$, a pump photon of wavelength λ_1 is absorbed. The probe wavelength λ_2 is tuned to ionize A, and this wavelength can also ionize the molecule AB (V_2^+). The observed change of the A^+ translational-energy distribution with the delay time reflects the time evolution of the total available energy from E_{avl}^+ at $t = 0$ to E_{avl} at $t = t_f$, i.e., mapping out the evolution of the nuclear separations from the initial reactants to final products. (b) Typical femtosecond pump−probe scheme for studying transition states and products using the LIF method. At $t = 0$, a pump photon of λ_1 is absorbed by the vertical transition from the ground-state V_0 to the excited-state V_1. To detect the final product or the transition-state species, the probe wavelength needs to be tuned to resonate with A* or AB** (V_2).

value of v is less than the v_d, and the observed KETOF distribution terminates between v and $-v$. As shown in Figure 4b, the higher the recoil speed, the stronger the v_{xy} discrimination and the sharper the observed KETOF distribution. This method was used to study the dissociation of IBz, a reaction with two-mode excitation, with a 5-mm-diameter discrimination aperture to reject ions with high-velocity components of $v_{xy} \geq v_d = 110$ m/s under our operating conditions.

III. Methodology

In this section, we describe the approach used in our studies for detecting transition states and final products simultaneously using only one probe femtosecond pulse. The concept is illustrated in Figure 5a, along with the original methodology of femtosecond transition-state spectroscopy,[26] shown in Figure 5b for comparison. For simplicity, we first consider a diatomic molecule AB prepared on a repulsive potential-energy surface (V_1) by absorbing one pump photon and finally dissociating into A and B. In the LIF study,[26] another femtosecond pulse is tuned to be resonant with the transition between the ground-state A and the excited-state A*. By observing the fluorescence from A* while varying the pump−probe delay time, we measure the dissociation time. On the other hand, to detect the transition-state evolution of $AB^{*\ddagger}$, the probe wavelength needs to be changed to match the transition between $AB^{*\ddagger}$ and $AB^{**\ddagger}$, that is, between V_1 and V_2, as shown in Figure 5b. The whole transition-state region can be probed if a continuum tuning is made.

Here, instead of observing the fluorescence by tuning the probe wavelength, we tune the probe laser to ionize A through a single or multiphoton process; typically A is ionized by REMPI. This way, and simultaneously, the complex $AB^{*\ddagger}$ could also absorb probe photons, through REMPI/MPI, to reach the ion state(s). In Figure 5a, this ion state is sketched as a repulsive state (V_2^+) as an example. The resulting cation AB^{+*} finally fragments into $A^+ + B$. By varying the delay time between the probe and the pump, we can observe the dynamics of transition states and final products, at the same time, using one wavelength for the probe and only resolving the kinetic energy.

At zero delay time, the observed translational energy of A^+ is determined by the total available energy $E_{avl}^+(t_0)$ on the excited ionic repulsive PES. When the wave packet moves into the transition-state region and is probed at a delay time of $t^\ddagger$, the final A^+ translational energy results from two parts: one contribution is from the available energy $E_{avl}(t^\ddagger)$, gained by the neutral complex AB* during the evolution from t_0 to $t^\ddagger$, and the other is from the excited ionic potential contribution, $E_{avl}^+(t^\ddagger)$, as shown in Figure 5a. If the ionic repulsive PES is deeper than the neutral one, the addition of both contributions is smaller than the initial ionic total available energy $E_{avl}^+(t_0)$ because some part of the photon energy is converted into the electron kinetic energy at $t^\ddagger$, and the observed translational energy of A^+ at $t^\ddagger$ is smaller than that at t_0. When the reaction is complete, the A^+ translational energy is the exact reflection of the A translational energy, which is obtained from the energy release of dissociation of AB*, that is, $E_{avl}(t_f)$. This total available energy $E_{avl}(t_f)$ is the least amount of energy channeled to the translational energy of A^+. *By following the change of the total available energy, that is, the time evolution of the* A^+

translational energy, the dissociation dynamics from the initial transition state to the final products can be studied.

For example, in our studies of the iodide (RI) molecular dissociation, the probe wavelength was set at ~304.5 nm to ionize the I (and I*) atoms through 2 + 1 REMPI (three photons). Most iodide molecules would be ionized by absorption of one pump photon and two probe photons (total of 12.61 eV), and the absorption of one more probe photon will result in reaching the excited ionic electronic state(s). As mentioned above, the I^+ translational-energy distribution at short times is dependent on these excited ionic states. In fact, for many systems the states reached by three probe photons may include some bound excited ionic states by ejecting an electron that carries away the excess energy. These ions in bound states proceed either to predissociate to form R + I^+(and R^+ + I), which is a long time-scale process ranging from picoseconds to nanoseconds, or to radiatively decay into the ground-state RI^+. So the initial $E_{avl}{}^+(t_0)$ could be equal to or less or larger than the final $E_{avl}(t_f)$ depending on the excited ionic PESs reached at the initial configuration. This can be easily determined from the I^+ speed distribution limits at t_0 and t_f.

In addition, the I^+ KETOF distribution at t_0 gives some information about the ion-fragmentation dynamics. At t_f, the KETOF distribution reflects the initial alignment by the pump pulse polarization. If the KETOF distribution at t_0 is similar to that at t_f, the ion fragmentation should be very prompt and preserves the initial alignment, and the excited ionic PES is effectively repulsive. Conversely, if the ion fragmentation is a long time process, the observed KETOF distribution at t_0 should be isotropic and the rotational motion destroys the initial alignment, indicating that the excited ionic state is bound in nature.

In our studies, $E_{avl}{}^+(t_0)$ was found to be larger than $E_{avl}(t_f)$ for I_2 and HgI_2. For ICN and CH_3I both $E_{avl}{}^+(t_0)$ and $E_{avl}(t_f)$ are almost equal, and for IBz, $E_{avl}{}^+(t_0)$ is less than $E_{avl}(t_f)$. However, the I^+ KETOF distribution shapes resulting from transition states and final products are always different. As shown in section IV, transition-state probing usually results in a broader distribution around $v_z = 0$ with fewer features due to the various ion fragmentations, but for products, the I^+ KETOF distribution has sharp structures relating to the initial alignment and the unique energy release of dissociation. As long as the PESs for the neutral and the ionic species are different, we are able to follow the change of the total available energy to obtain the dissociation dynamics, from the initial to the final configuration of the reaction.

This approach, which we utilized in earlier studies,[8] is analogous to the recently reported anion femtosecond photoelectron spectroscopy from Neumark's group.[27] There, a femtosecond pulse was used to excite a ground-state anion to a repulsive excited state and another femtosecond pulse was employed to detach an electron from the anion. When the wave packet is mapped onto accessible neutral surfaces, the evolution of the resulting different kinetic-energy electrons directly reflects the dissociation dynamics of the anion. Here, we follow the evolution of the kinetic-energy-resolved cations by accessing ionic surfaces to study the dissociation dynamics of neutral molecules. Both methods use only one probe laser to detect the transition states and final products.

IV. Results and Discussion

In this section, we discuss the different systems studied here. They range in the level of complexity from diatomics to polyatomics, from direct-mode to complex-mode, from one-center to two-center to four-center, and from unimolecular to bimolecular reactions.

The diatomic iodine was first examined owing to its simplicity. Since all the available energy is released into translational energy of the two I atoms, it represents the case of no coupling to other degrees of freedom, such as vibrational and rotational motions. This is not the case for polyatomic RI or RI_2. Furthermore, we used this system to calibrate the instrumental response for kinetic-energy resolution in measuring the KETOF distribution. In general, by knowing the excitation energy for a polyatomic molecule, say R−I, the energy disposal after breaking the R−I bond follows the conservation of the total energy:

$$E_{avl} = h\nu + E_I(\mathrm{RI}) - D_0^0(\mathrm{R{-}I}) = E_I(\mathrm{R}) + E_T \qquad (7)$$

where E_I(RI) is the initial internal energy of the parent molecule, D_0^0(R−I) is the dissociation energy from the ground-state parent to the ground-state fragments, and E_I(R) is the internal energy of the fragment R gained during the dissociation. The iodine atom can be in either the ground I or excited I* spin−orbit state; eq 7 is for I release, and for I*, E_T will be reduced by 7605 cm^{-1}.

By measurement of the center-of-mass (c.m.) translational-energy release E_T, the internal-energy distribution of R can be obtained following eq 7. For the I_2 dissociation, E_I(R) = 0. The c.m. translational energy can then be obtained from the translational energy of I atoms, E_T^I:

$$E_T = E_T^I \frac{M}{M-m} \qquad (8)$$

where M is the mass of the parent molecule and m is that of the I atom.

A. One-Bond Breakage: Direct-Mode Reactions. *(1) I−I: Pure-Translation Motion.* The dissociation of I_2 in the A state was studied by using a 690-nm pulse. This system was examined in photofragment translational spectroscopy (PTS) experiments by Wilson and co-workers.[28] At our wavelength, the contribution from the B state is essentially eliminated (see below)[29] and the system dissociates into two iodine atoms in the ground state:

$$I_2 + h\nu \rightarrow [\mathrm{I{\cdots}I}]^{*\ddagger} \rightarrow \mathrm{I} + \mathrm{I} \qquad (9)$$

The time evolution of the I^+ KETOF distributions is shown in Figure 6A ($\chi = 90°$). Notice that the shape changes with the delay time. At the early delay time (−200 fs), the KETOF signal is a broad, symmetric distribution around $v_z = 0$ and extends to $v_z = \pm 800$ m/s. The predicted v_z value by three-photon probing of the A state is ±1240 m/s, so part of the photon energy is converted to the electron kinetic energy. The symmetric distribution around $v_z = 0$ implies that the probed excited ionic state has a bound character around 12.84 eV (3.56 eV above the ground-state $I_2{}^+$) and the predissociation of iodine ions takes long time. At later times (after 600 fs), the I^+ KETOF distribution remains unchanged and the v_z value changes to ±485 m/s. The time evolution of v_z values from the initial 800 m/s to final 485 m/s reflects the change of the total available energy, as predicted in section III for the case of $E_{avl}{}^+(t_0) > E_{avl}(t_f)$.

The χ dependencies of the v_z distributions are given in Figure 6B for a fixed delay time (6 ps). These KETOF distributions clearly show a perpendicular transition for the A-state excitation, as expected.[29] The speed distribution derived from the KETOF

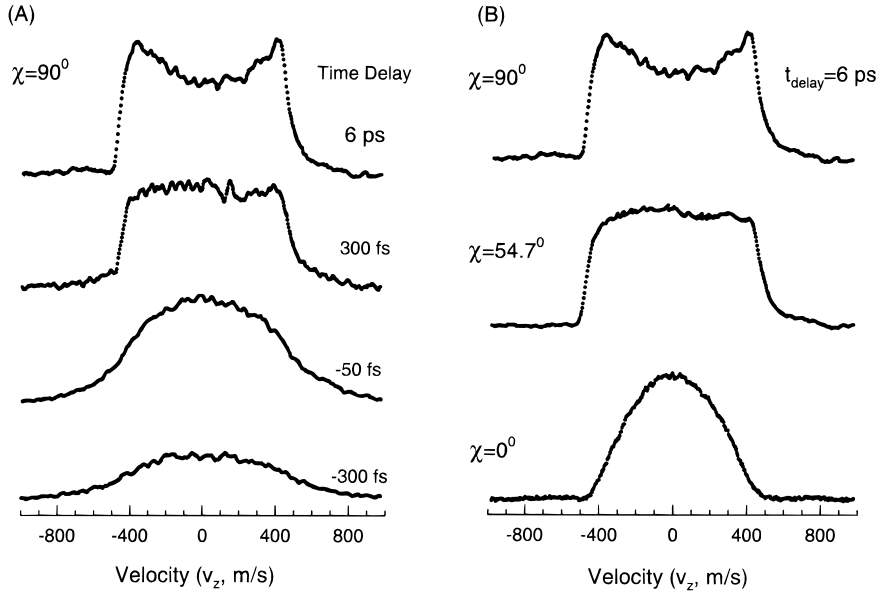

Figure 6. (A) Femtosecond-resolved I^+ KETOF distributions arising from the dissociation of I_2 at $\chi = 90°$. Note the significant change in shape with the pump−probe delay time. (B) I^+ KETOF distributions for the different χ's at a fixed delay time of 6 ps, which shows a perpendicular transition for the A-state excitation of I_2 at 690 nm.

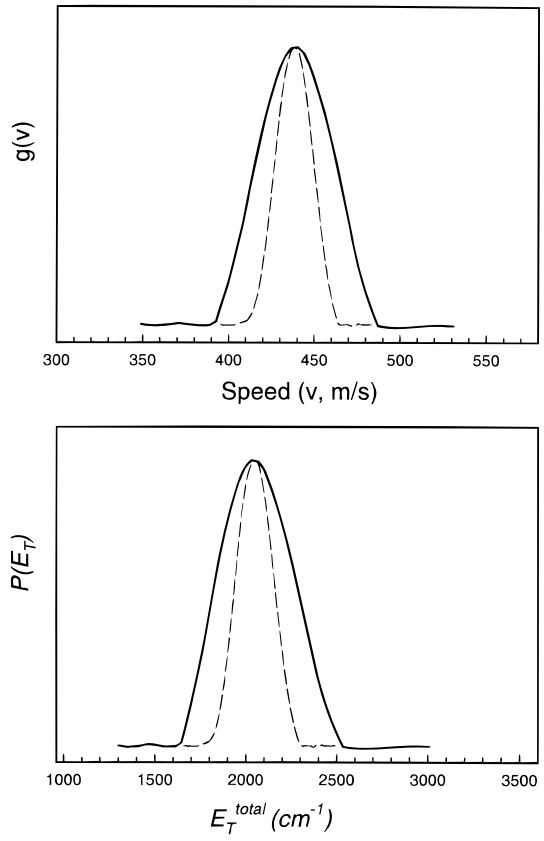

Figure 7. Upper panel: speed distributions of iodine atoms (from I_2) deduced from the I^+ KETOF signal for $\chi = 54.7°$ at 6 ps (solid line) and from the pump−pulse bandwidth (dashed line). The instrument resolution is obtained to be within ±15 m/s at a speed of 440 m/s from comparison. Lower panel: corresponding c.m. translational-energy distributions from the dissociation of I_2, which equals the total available energy.

distribution at the magic angle is shown in Figure 7, together with the c.m. translational-energy distribution. The corresponding speed and translational-energy distributions derived from the pump laser spectrum (dashed line) are also presented for comparison. Since the total available energy is channeled only into the translational energy of two iodine atoms, the instrument resolution at the speed of 440 m/s is obtained to be within ±15 m/s. The higher the speed, the better the expected resolution.

To obtain the temporal behavior, we gated the high-velocity ($340 \le v_z \le 490$ m/s) and low-velocity ($0 \le v_z \le 120$ m/s) portions of the I^+ KETOF distribution at $\chi = 90°$ while varying the delay time. The two transients are shown at the bottom of Figure 8. Each transient is composed of two components with different weights but has the same dynamics; one is from the iodine ion fragmentation and the other results from the neutral-iodine dissociation. By measurement of time zero and the response function in situ, the transient was best fitted by a (coherent) delayed, 240 fs, rapid rise and a decay component with a lifetime of 65 fs, as shown in the top of Figure 8. The observed 240-fs shift is the bond-breaking time for separating two I atoms and describes the coherent motion of the wave packet prepared above the dissociation limit on the A-state potential surface. The decay transient actually reflects the evolution of the parent $I_2{}^{*‡}$ in the transition state. This picture is also consistent with the observed I^+ KETOF evolution. The measured decay time is shorter than the bond-breaking time because the wave packet escapes out of the Franck−Condon region before the I atom is totally liberated.

(2) I−CN: Translation and Rotation Motions. The dissociation of ICN was the first gas-phase reaction studied by femtosecond clocking.[26,30,31] At 306-nm excitation, the bond-breaking time was obtained to be 205 fs by detection of the CN product through LIF. The transition-state lifetime was estimated to be ~50 fs. Here, we resolve the I* and I channels with the dissociation times, energy partition, and angular distributions.

It is now well established that following electronic excitation via the A continuum (n → σ^* transition), ICN dissociates through two exit channels, leading to spin−orbit excited- and ground-state iodine atoms I* and I, respectively:

$$\mathrm{ICN} + h\nu \rightarrow [\mathrm{I}\cdots\mathrm{CN}]^{*‡} \rightarrow \mathrm{I}^*/\mathrm{I} + \mathrm{CN} \qquad (10)$$

Time-integrated spectral studies,[32−39] by use of a variety of methods such as PTS,[32,38] LIF,[33,34] Doppler spectroscopy,[35,37]

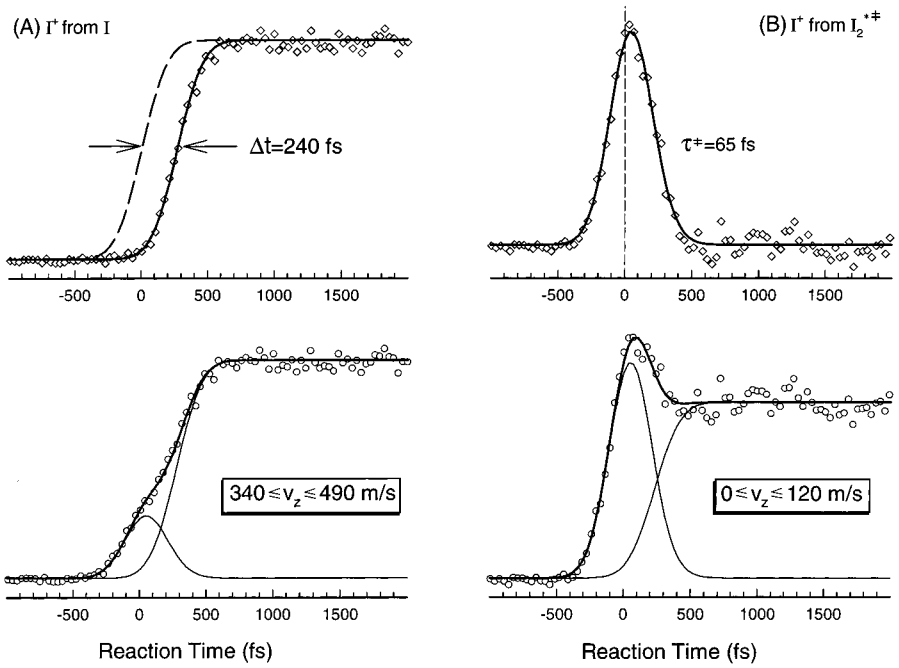

Figure 8. (A) I^+ transient obtained by gating the high-velocity portion in the I^+ KETOF distribution (bottom) of iodine dissociation. By measurement of time zero and pump−probe correlation in situ (dashed line), the transient is best fitted by a small decay component ($\tau^{\ddagger} = 65$ fs) and a large 240-fs delayed one. The decay I^+ signal is due to excited I_2^+ fragmentation and reflects the transition-state $I_2^{*\ddagger}$ dynamics and the delayed one, which is shown at the top, after subtraction of the small decay signal, results from the neutral I_2 dissociation. (B) I^+ transient obtained from collecting the low-velocity portion in the I^+ KETOF distribution (bottom). The signal is fitted as in (A) by two components: a 65-fs lifetime decay and a 240-fs delayed rise. The decay signal is separately shown at the top after subtraction of the contribution from the neutral I_2 dissociation.

and REMPI-TOF,[39] have provided many detailed features of the dynamics for both channels.

Briefly, the I*/I branching ratio is dependent on the excitation wavelength and the I* yield peaks at ∼260 nm; it falls off at shorter wavelengths as well as at longer ones. The vibrational excitation of the CN fragment is low (cold), except in the low-energy region (350−290 nm) where several percent of CNs are vibrationally excited. However, the rotational excitation of CN is found to be very rich (hot) in the I channel (up to $N \approx 60$), whereas it is rotationally cooler in the I* channel, for the medium energy range (248−290 nm). In the low-energy region, where the I* channel is not energetically accessible, the product rotation population shows a single Boltzmann distribution. The average anisotropy parameter β of the I* channel is larger than that of the I channel. The transition moment is observed to be a mixture of parallel and perpendicular components, especially at shorter and longer wavelengths.

Goldfield et al.[40] developed a two-surface empirical model for the ICN dissociation in the A continuum. In their model, the initial excitation is a purely parallel transition to the potential surface ($^3\Pi_{0+}$), which correlates with the I* + CN channel, followed by a transition through nonadiabatic interaction to the surface ($^1\Pi_1$), which correlates with the I + CN channel. The $^3\Pi_{0+}$ surface is repulsive in R(I−CN) and has a minimum at $\theta = 0°$ in the θ coordinate (bending angle). This results in the collinear configuration in the dissociation process, leading to low rotational excitation in CN fragments. The second surface is also repulsive in R but has a minimum in θ at $\theta = 27°$. The large torque at small θ favors a bent configuration during the dissociation and leads to high rotational energy for the final fragment. The results from classical-trajectory calculations and quantum-mechanical studies based on this model agree well with some experiments, but large deviations still exist.[40−46]

Recently, Morokuma and co-workers[47] developed ab initio 3D PESs of $^3\Pi_1$, $^3\Pi_{0+}$, and $^1\Pi_1$ excited states and found that all PESs involved in dissociation are *bent* near the Franck−Condon region. Classical-trajectory and time-dependent quantum-mechanical calculations performed on these PESs have produced results that are in good agreement with various experimental findings.[47−51] The absorption is a mixture of parallel and perpendicular transition; $^3\Pi_1$ and $^1\Pi_1$ have perpendicular transitions, and $^3\Pi_{0+}$ belongs to a parallel transition. The rotational excitation of the CN fragment is related to the shape of PESs with respect to the bending angle. The higher rotational component in the I channel is attributed to the larger energy gradient of $^1\Pi_1$ with respect to the bending angle. The rotational excitation in the I channel at long wavelengths (290−350 nm) only emerges from the $^3\Pi_1$ surface. The product CN vibrational excitation on $^3\Pi_{0+}$ and $^1\Pi_1$ becomes suppressed, while that on $^3\Pi_1$ becomes slightly significant (from the shape of PES with respect to the C−N distance). On the surface $^3\Pi_{0+}$, a potential well (3855 cm^{-1}) is found along the reaction I−CN coordinate at 2.59 Å.

We performed the femtosecond-clocking and fs−KETOF experiments to obtain the dissociation time, energy partitioning, and the anisotropy parameter. The femtosecond-resolved I^+ KETOF distributions at $\chi = 0°$ are shown in Figure 9A and the χ dependencies for a fixed delay time (2 ps) in Figure 9B. All distributions extend to $v_z \approx \pm 600$ m/s, but the shape changes dramatically. At the earlier delay time (−290 fs), a symmetric distribution around $v_z = 0$ was observed. As in the case of I_2, this reflects that the excited ionic PESs reached by three-photon probing have a bound character around 15.06 eV (4.15 eV above the ground-state ICN^+) and that the predissociation takes a longer time compared with the rotational period of the ion parent. Some photon energy is converted into electron kinetic energy because the expected v_z value is ±880 m/s by absorption of three probe photons. At later delay times, the distribution shows the clear double splitting for both I* and I channels, which means that the excitation at 277 nm is a *purely* parallel transition.

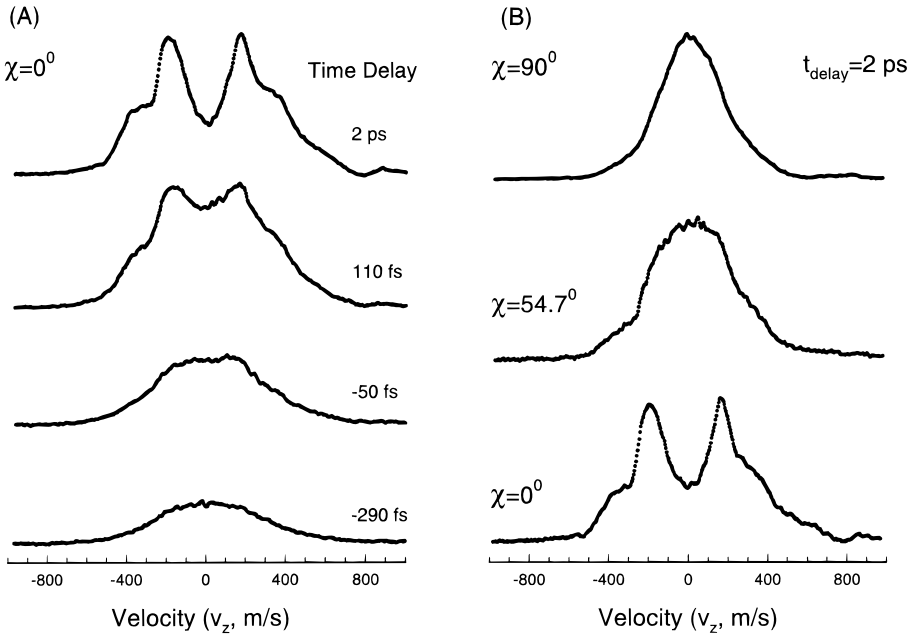

Figure 9. (A) Femtosecond-resolved I^+ KETOF distributions from the dissociation of ICN at $\chi = 0°$. At the early delay time, the I^+ signal is from excited ICN^+ fragmentation, and at the later time, it results from the neutral iodine atoms. The distribution remains the same after 600 fs. Note the dramatic change in shape with the delay time. (B) I^+ KETOF distributions for the different χ's at a fixed delay time of 2 ps, which show a pure parallel transition for excitation of ICN at 277 nm.

This is also clear in the distribution at $\chi = 90°$ in Figure 9B. The deduced β values further support this finding, as discussed below.

The speed distribution for the iodine product derived from the magic-angle KETOF distribution and the corresponding c.m. translational-energy distribution with assignments of rotational excitation for the CN fragment are shown in Figure 10. The speeds from the I* and I channels do reach the limits determined by the total available energy for each channel (285 m/s for I* and 570 m/s for I). The I* quantum yield is about 60%, consistent with the value reported by Leone.[36] The translational-energy release $\langle E_T \rangle / E_{avl}$, is 70% for the I* channel and 63% for the I channel, which corresponds to 30% and 37% of the available energy (764 cm^{-1} for I* and 3756 cm^{-1} for I) channeling into rotational excitation in the I* and I channels, respectively. The rotational distributions peak at $N = 20-25$ for the I* channel and $N = 45-55$ for the I channel. These assignments are in agreement with the results from the time-integrated experiments.[35,37]

By simulating the KETOF distribution at $\chi = 0°$ using the derived speed distribution, we deduced the β distribution, which is also shown in Figure 10. All β values are positive, thus indicating that *only* the parallel transition state $^3\Pi_{0+}$ was excited at 277 nm. (Recent work[37b] has concluded a pure parallel transition for 308-nm excitation, contrary to the expectation of a mix of parallel and perpendicular transitions at long wavelengths.) Therefore, the I product results from the nonadiabatic interaction from $^3\Pi_{0+}$ to $^1\Pi_1$. Most products have very high β values (≥ 1.6) even with high rotational excitation. During the rapid dissociation, since the rotation of ICN plays a minimal role, the rotational excitation should result from the bent configuration of the excited surface, as suggested by the ab initio calculations.[47,49] For both I* and I channels, the CN fragments in the distribution at higher rotational excitation have decreased β values, which indicates that some large-amplitude bending motion is involved during the dissociation.

The χ dependencies of the transition-state I^+ KETOF distributions and the deduced speed function are given in Figure

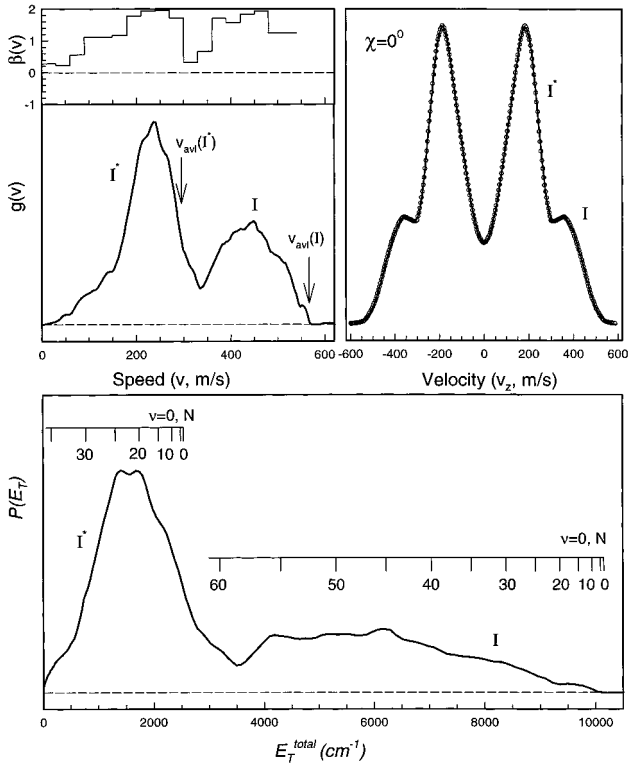

Figure 10. Speed distribution deduced from the I^+ KETOF signal at the 2-ps delay time for $\chi = 54.7°$ (top left) for the ICN reaction. Both I and I* channels are clearly identified and reach their speed limits (see arrows). The corresponding anisotropy distribution is shown at the top, which is obtained by a nonlinear-least-squares fit of the parallel polarization KETOF signal (top right) using the derived speed distribution. All β's are positive, and the average is larger than 1.6. The c.m. translational-energy distribution with the corresponding rotational excitation of CN is shown at the bottom.

11. The speed distribution is very broad, and the deduced β values are small, also shown in Figure 11. The average β value is about 0.5, much smaller than that (≥ 1.6) for the final product. As predicted in section III, this small value reflects the dynamics

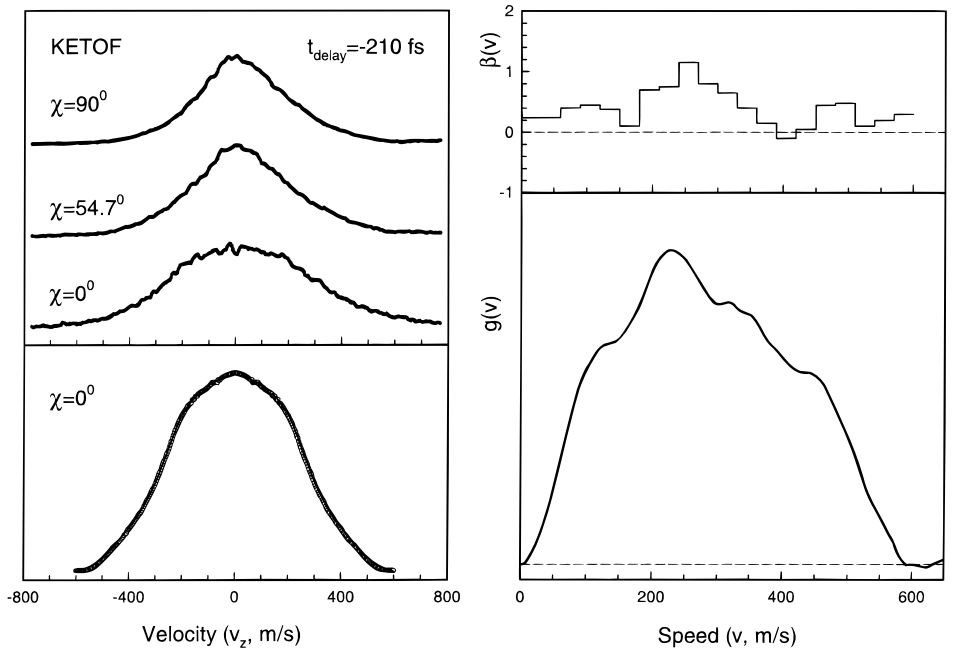

Figure 11. I^+ KETOF distributions (ICN reaction) for the different χ's at the early delay time (−210 fs) shown at the top-left side. Note the difference when comparing with Figure 9B. The speed distribution derived from the magic-angle KETOF distribution at −210-fs delay time is shown in the bottom-right side, which is very broad as expected for ion fragmentation. The anisotropy distribution is shown at the top-right, which is obtained by a nonlinear-least-squares fit of the parallel polarization KETOF signal (bottom left) using the deduced speed distribution. The average anisotropy is about 0.5, much smaller than that from the neutral ICN dissociation (1.6).

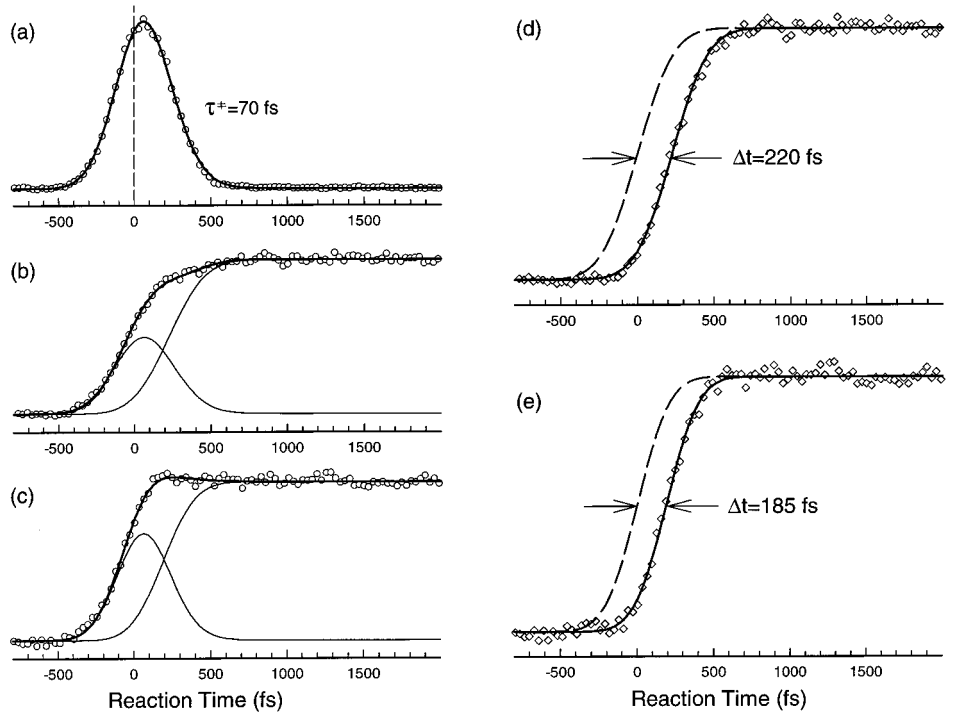

Figure 12. (a) Transient obtained by monitoring the signal of the ICN^+ mass channel. By measurement of the response function in situ (dashed line in parts d or e), the transient was best fitted by a single-exponential decay with a 70-fs lifetime. (b, c) Transients obtained by gating the I* ($150 \leq v_z \leq 300$ m/s) and I ($380 \leq v_z \leq 580$ m/s) channels. Both transients were fitted by two components: one as a decay signal from ion fragmentation around $t = 0$ with a lifetime of 70 fs and the other as a shift, rapid rise. (d, e) Transients with 220- and 185-fs coherent shifts for the I* and I channels, respectively, were obtained by subtracting the contributions from the transition-state species. Note that measuring the time zero and the cross correlation in situ is a key for accurate fitting of these transients.

of the ion fragmentation and implies that the excited ionic states reached by three-photon probing have a bound character and the predissociation takes a relatively long time in order to reduce the initial alignment.

The dissociation dynamics was selectively resolved by performing the gating experiments. The parent mass transient is shown in Figure 12a. By use of the known time zero and response function, the transient was deconvoluted by a decay signal with a 70-fs lifetime, which reflects the transition-state dynamics of $ICN^{*\ddagger}$. This lifetime can only be obtained by sampling all transition-state configurations through this probing scheme. By gating the high velocities of I^+ KETOF distribution,

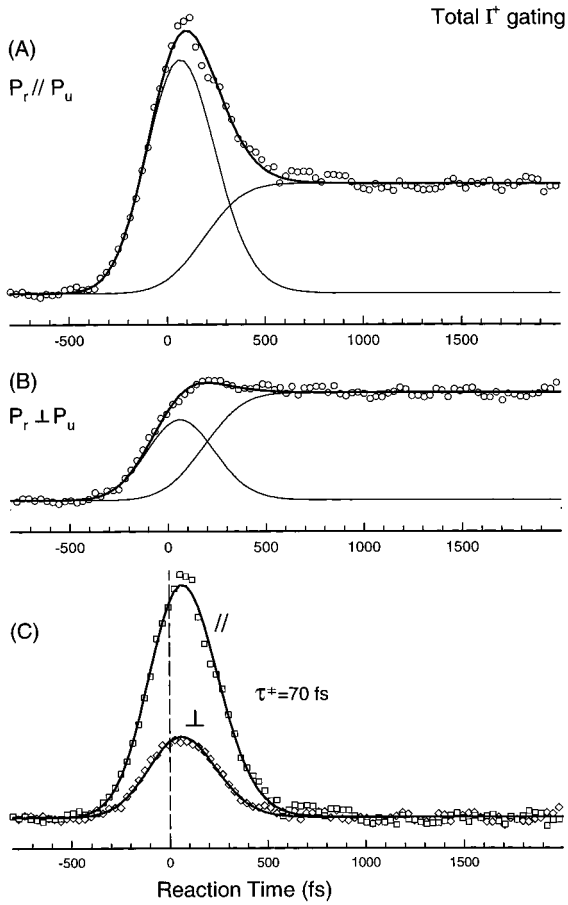

Figure 13. (A, B) Transients obtained by collecting all I^+ signal corresponding to the pump polarization parallel ($\chi = 90°$) and perpendicular ($\chi = 0°$) to the probe, respectively (ICN reaction). Both transients are fitted by one component from the transition-state contribution (70-fs lifetime) and a shift, rapid rise from the neutral ICN dissociation, as in Figure 12. (C) Transients obtained by subtraction of the shift rise component from (A) and (B). Both transients represent the decay dynamics of the transition state with the different pump−probe polarization combinations. As predicted from the theory, the signal from the parallel is 3 times larger than from the perpendicular one.

$150 \leq v_z \leq 300$ m/s and $380 \leq v_z \leq 580$ m/s for I* and I, respectively, we obtain the dissociation times for forming the I* and I products, as shown in parts b and c of Figure 12, respectively. Both transients include a contribution from fragmentation around $t = 0$. Therefore, these two transients were fitted by a (coherent) delayed rapid rise, which are shown in parts d and e of Figure 12 for I* and I, and a decay component (70-fs lifetime) from the transition state. The I* atoms were born after 220 fs from time zero, and the I atoms take 185 fs to be liberated. Although the rotational dependence of the dissociation times was found, both from the experiments[26] and theoretical calculations,[52] the observed 220 fs here for I* and 185 fs for I represent the average dissociation times for rotationally populated CN fragments. The longer dissociation time for I* is consistent with the smaller terminal speed.

We also gated the total I^+ KETOF distribution, that is, collected all signals. The transients are shown in parts A and B of Figure 13 with the corresponding pump polarization parallel ($\chi = 90°$) and perpendicular ($\chi = 0°$) to the probe polarization, respectively. By subtraction of the contribution of the final iodine products (the contribution should be the same for these two cases, as observed in the experiment, and is independent of the pump or probe polarization), the residual transients were obtained (Figure 13C). These are purely from the probing of the transition state ICN*‡ for different polarization combinations. With the pump polarization being parallel to the probe polarization, the transition-state transient is 3 times larger than that when the pump polarization is perpendicular. This observation is completely consistent with the theoretical prediction.[53]

(3) CH_3−I: Translation and Vibration Motions. The dissociation dynamics from the A-band absorption ($n \rightarrow \sigma^*$ transition) has been extensively studied[54−64] and new insights have been gained. The dissociation steps are

$$CH_3I + h\nu \rightarrow [CH_3\cdots I]^{*\ddagger} \rightarrow CH_3 + I^*/I \qquad (11)$$

Various experimental techniques such as PTS,[55,57] IR emission[56] and absorption,[61] REMPI-TOF,[58,63] Raman,[54] photofragment imaging,[59] and ZEKE[62] have been used to resolve the product-state distributions (rotational and vibrational) and branching ratio of I*/I and to address the nonadiabatic interaction during the dissociation. For the wavelength we used (277 nm), only one electronic state, $^3Q_{0+}$, is mainly excited through a parallel transition, as observed in ICN, which dissociates to CH_3 and I*. The observed I atoms suggest significant nonadiabatic interactions between $^3Q_{0+}$ and $^1Q_1$ states during the course of dissociation because the latter, $^1Q_1$ state, correlates to the CH_3 + I asymptote by a perpendicular excitation.

Although some small excitation in the C−H symmetric stretch (ν_1) of the CH_3 fragment has been reported, only the umbrella mode (ν_2) of CH_3 was found to be strongly excited in either the I* or I dissociation channel. This is consistent with the structural change, from being with nearly tetrahedral angles in CH_3I to being planar in CH_3. The rotational distribution for motion about the axis perpendicular to the C_3 axis of the CH_3 fragment is relatively hot in the I channel but very cold in the I* channel. Kinsey and co-workers[54] have concluded from their resonance Raman spectroscopy experiments that during the dissociation the C−I bond extension initially takes place to some extent before the subsequent umbrella motion starts. The dissociation time estimated by photofragment anisotropy measurements,[65] picosecond real-time studies,[66] and Raman scattering[54] of dissociating CH_3I is less than 500 fs.

Theoretically, Shapiro and Bersohn[67] suggested a model that considers a linear, pseudotriatomic molecule; the umbrella motion of the CH_3 moiety was approximated by a stretch motion between C and H_3. Both quantum and classical-dynamical studies based on this model have produced promising results.[67−69] Very recently, an ab initio 6D (all coordinates except the three C−H stretches)[70] and full 9D PESs[71] have been reported by Morokuma and co-workers. These potentials were used to perform classical trajectories,[70,71] 3D-wave-packet dynamics,[72] including rigid bending of H_3−C−I, and 5D-multiconfiguration time-dependent Hartree method calculations.[73] The results are in good agreement with various experimental observations.

The rotational excitation in the I channel is closely related to the shape of the PES with respect to the bending angle outside the conical intersection of $^3Q_{0+}$ and $^1Q_1$, that is, there might exist a small well for the $^1Q_1$ surface near the linear geometry. The vibrational excitation is determined by the shape of the PESs with respect to the umbrella angle and its coupling with the C−I coordinate. The $^3Q_{0+}$ surface has a shallow well (1710 cm^{-1}) along the reaction C−I coordinate at 3.3 Å. The observed hotter vibrational excitation in the I channel is due to the sudden change of the reaction coordinate from $^3Q_{0+}$ to $^1Q_1$ at the conical interaction. The quantum-wave-packet calculations gave a 75-fs dissociation time for a C−I separation of ∼5 Å.[72] Here, we are able to clock the femtosecond dissociation dynamics.

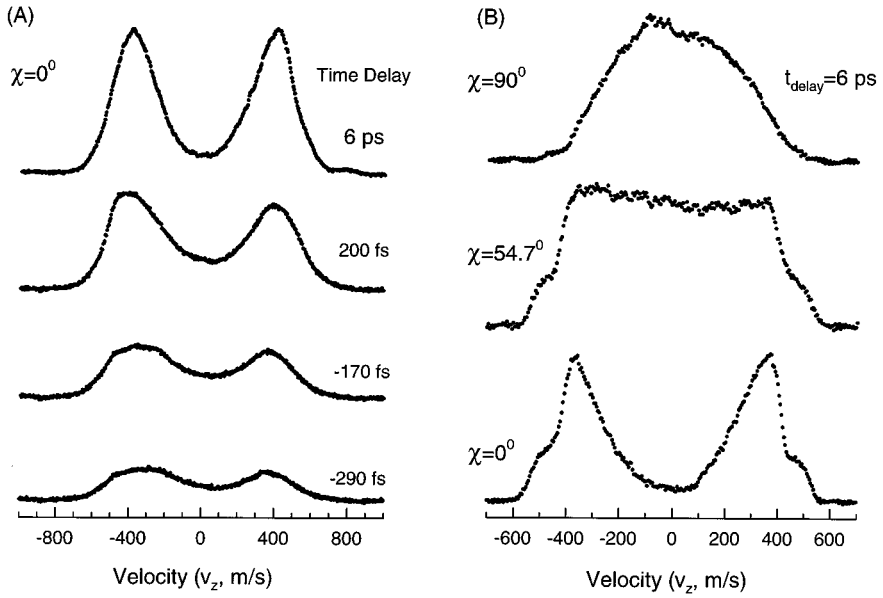

Figure 14. (A) Femtosecond-resolved I^+ KETOF distributions from CH_3I dissociation at $\chi = 0°$. The signal at early times results from excited CH_3I^+ fragmentation. After 600 fs, the distribution is unchanged. Unlike I_2 and ICN, all distributions are similar in shape. (B) I^+ KETOF distributions from the different χ's at 6-ps delay time, which shows a pure parallel transition for excitation of CH_3I at 277 nm.

The femtosecond-resolved I^+ KETOF distributions are shown in Figure 14A ($\chi = 0°$) and the angular (polarization) dependence (χ) at the 6-ps delay time is in Figure 14B. All fs−KETOF distributions extend to $v_z \approx \pm 600$ m/s and have double peaks. Unlike I_2 and ICN, the excited ionic potential surface reached by three-photon probing is similar to the neutral one and is repulsive around 15 eV (5.46 eV above the ground-state CH_3I^+), that is, the ion fragmentation is very prompt, although the distributions from the transition state have broader peaks and lie closer to $v_z = 0$. The predicted v_z value by absorption of three probe photons at $t = 0$ is ± 791 m/s, larger than the observed value. Therefore, some portion of photon energy is converted to the electron kinetic energy. The fs−KETOF distributions show no change after 600 fs, which means the termination of the bond breaking.

The product speed distribution is derived from the measured I^+ KETOF distribution at the magic angle and taken at times after the bond breaking. The result is shown in Figure 15, also with the c.m. translational-energy distribution. The first peak is measured to be at ~410 m/s, and this speed corresponds to the spin−orbit excited-state I* dissociation channel. The second peak located at ~530 m/s corresponds to the ground-state I dissociation channel. If all available energy is channeled into translational motion, the expected speeds do reach the limit values indicated by the arrows in Figure 15 (440 m/s for I* and 587 m/s for I). The average translational energy release $\langle E_T \rangle / E_{avl}$ is found to be 87% for I* and 81.7% for I. The I* quantum yield is measured to be ~65%, which agrees with the values reported by others.[55,56] When the translational-energy release is known, the internal energy distribution of CH_3 can be obtained. The corresponding umbrella excitation is marked in Figure 15; for the I* channel, the vibrational peak distributions are $\nu = 1, 2$, and for the I channel, the peaks shift to $\nu = 4-5$. These observations are consistent with those reported by Lee's group[55] but 1−2 quanta higher (for the I channel) than the results reported in ref 58.

From the speed distribution and the I^+ KETOF distribution, obtained at the parallel polarization, we deduced the anisotropy parameter $\beta \approx 1.85$ at 277-nm excitation, which is in good agreement with the values reported by Bersohn (1.81),[65] Houston (1.8),[58] Crim (1.9),[58] and others.[57] This also confirms that the observed I atoms are not from the direct excitation of the $^1Q_1$ state (perpendicular transition and $\beta \approx -1$) but are instead from the initial $^3Q_{0+}$ state (parallel transition) followed by a transition through nonadiabatic interactions to the $^1Q_1$ state. From β, Bersohn[65] deduced a lifetime of 70 fs. As shown below, femtosecond clocking gives a 125-fs dissociation time.

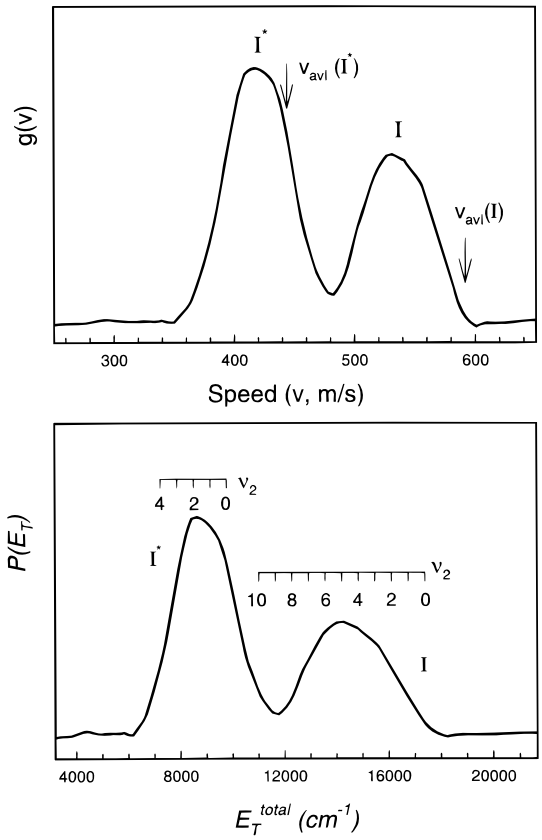

Figure 15. Speed distribution derived from the magic-angle I^+ KETOF distribution at 6-ps delay time (CH_3I reaction). Both I* and I channels are identified and reach their speed limits (see arrows on the upper panel). The c.m. translational-energy distribution with the corresponding vibrational excitation of CH_3 umbrella mode is shown in the lower panel.

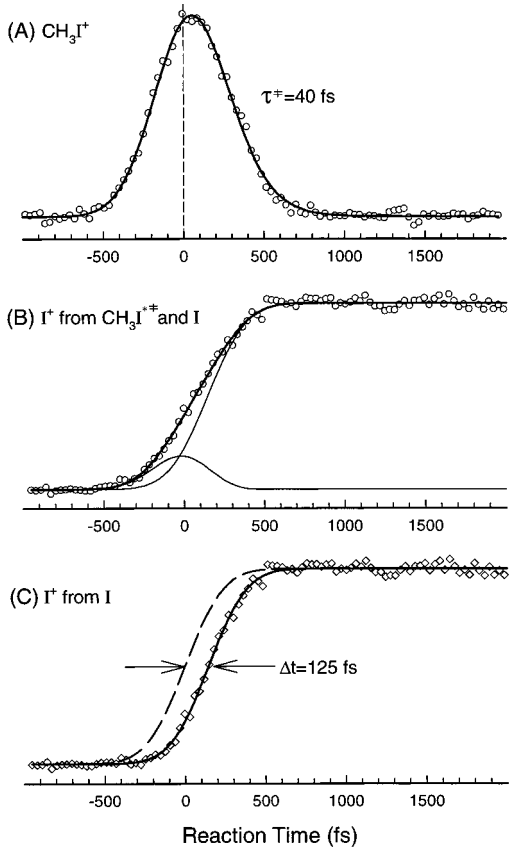

Figure 16. (A) Transient obtained by monitoring the signal of the CH_3I^+ mass channel. By measurement of the response function in situ (dashed line in C), the signal is best fitted by a single-exponential decay with a lifetime of 40 fs. (B) Transient obtained by gating the high v_z values ($500 \leq v_z \leq 380$ m/s) and fitted by a small decay component with a 40-fs lifetime and a shift, rapid rise. (C) Transient with a 125-fs coherent shift obtained by subtraction of the small decay signal from (B).

The temporal transient is shown in Figure 16B by gating the high v_z values ($500 \leq v_z \leq 380$ m/s). This transient includes a small component from the excited CH_3I^+ fragmentation ($I^+ + CH_3$), as in the cases of I_2 and ICN. The total parent mass signal is also gated, and the resulting transient is shown in Figure 16A, which reflects the transition-state dynamics. By measurement of time zero and the response function in situ, a 40-fs lifetime was deduced from Figure 16A. The result of Figure 16B was then uniquely fitted to a rapid-rise component with a 125-fs coherent shift, as shown in Figure 16C, and a small portion of the 40-fs lifetime transition-state signal. No attempt was made to separate the I* and I channels. The 125-fs dissociation time is longer than the values deduced from the β measurement[65] and the quantum-wave-packet calculations.[72] Measurements of the anisotropy (β) are sensitive only to the initial force (short distances), while real-time measurements probe the nuclear separation when fragments become free from the force field of each other (dissociation time).

B. One-Bond Breakage: Complex-Mode Reactions. The three systems (I_2, ICN, and CH_3I) presented in the above sections all involve direct-mode reactions in that the initial preparation is to a repulsive surface (or weakly bound surface). In other words, the energy is directly deposited into the bond that breaks and the system has no time to involve the multimodes of the complex in coordinates other than the reaction coordinate (see Figure 17). In this section, we study another case, complex-mode reactions, using iodobenzene as an example.

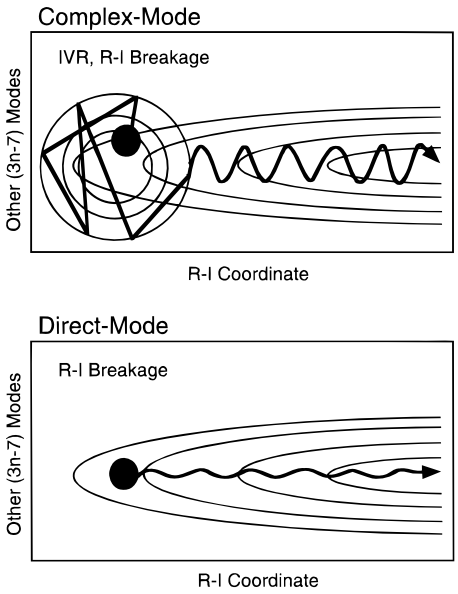

Figure 17. Schematic representation for the mechanism of direct-mode and complex-mode reactions.

$$C_6H_5I + h\nu \rightarrow [C_6H_5\cdots I]^{*\ddagger} \rightarrow C_6H_5 + I\ (I^*) \qquad (12a)$$

$$\rightarrow [C_6H_5{-}I]^{*\ddagger} \rightarrow C_6H_5 + I \qquad (12b)$$

At the wavelength we used (277 nm), two states[74] are excited simultaneously: one is a repulsive (n, σ^*) excitation in the C−I bond and the other is a bound (π, π^*) benzene-ring excitation. Through time−velocity correlation during the dissociation, we are able to separate the two dynamical channels: a direct-mode dissociation (eq 12a) due to the C−I repulsion and a complex-mode; electronic predissociation (eq 12b) arising from IVR in the benzene ring, which drives energy to the C−I coordinate.

Previous studies of the dissociation dynamics of IBz have been obtained from the PTS and resonance Raman scattering experiments. Bersohn's group[65,75] has measured β and found it to be lower than those observed for alkyl iodides, suggesting the presence of a predissociation channel. El-Sayed's group[76] introduced a state-selective method to determine the spatial and velocity distributions of the nascent ground-state iodine atoms using nanosecond lasers. Two distinct iodine velocity distributions were observed. One is a high velocity, narrow distribution that exhibits a high anisotropy. The other is a low velocity, broader distribution accompanied by a lower averaged anisotropy. Kinsey's group,[74] for excitation to the B continuum, related the Raman profile and its change to the initial dynamics and the activity of modes.

Measurements of the anisotropy give a limit for τ_{reac} being less or comparable to τ_{rot}, the average rotational time of the parent molecule. If $\tau_{reac} \geq \tau_{rot}$, the intermediate or long time dynamics is difficult to obtain.[74] Moreover, as pointed out by El-Sayed et.al.,[76] if IVR precedes C−I bond breakage, then inference can only be made provided that β can be related to the IVR process. Bersohn's study[75] gave an upper limit of τ_{reac} based on τ_{rot} of IBz as a clock. El-Sayed's group[76] assigned the high-velocity distribution to the rapid dissociation on the (n, σ^*) surfaces and the low-velocity component to the predissociation of the $^3(\pi, \pi^*)$ state. Using the molecular rotation as a clock, they were able to deduce a time scale for the IBz dissociation: the (n, σ^*) states dissociate much more quickly than the molecular rotation, whereas the predissociation in the $^3(\pi, \pi^*)$ states takes place on a time scale comparable to the

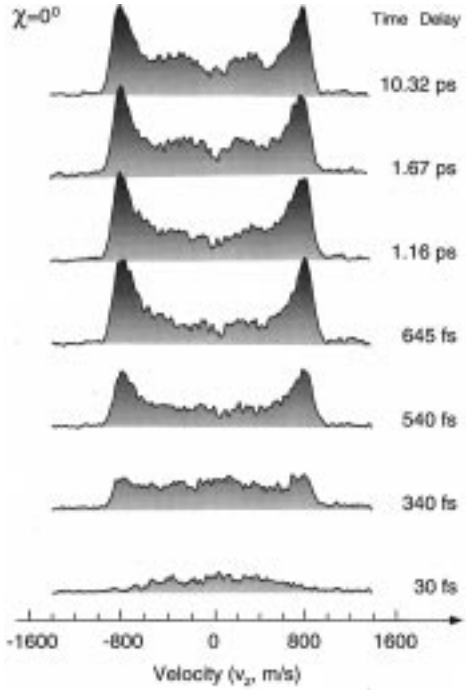

Figure 18. Femtosecond-resolved I^+ KETOF distributions for the dissociation of iodobenzene at $\chi = 0°$. The shading intensity is roughly proportional to the ion signal, for clarification purposes. The distribution only extends to ±800 m/s at the early delay times and reaches ±960 m/s at the later times. After ~2 ps, the distribution remains unchanged. Note that the signal around $v_z = 0$ grows more slowly than that of the high-v_z range.

time scale of the molecular rotation. Here, we are able to directly clock these two dissociation channels and focus on the studies of resolving the translational energy on the femtosecond time scale to separate the two reaction pathways and to characterize the dissociation dynamics.

Figure 18 shows the I^+ KETOF distributions ($\chi = 0°$) taken at different delay times. In these experiments, a small discrimination aperture (5 mm) was used in front of the MCP detector to eliminate the ions with $v_{xy} \geq 110$ m/s and to enhance the kinetic-energy resolution. At earlier delay times (≤30 fs), the KETOF distribution extends to $v_z = \pm 800$ m/s and is symmetric around $v_z = 0$. As observed in I_2 and ICN, the excited ionic states probed by three-photon absorption have a bound character around 14.43 eV (5.7 eV above the ground-state IBz^+). The expected value is $v_z = \pm 1387$ m/s from the three-photon probing. Therefore, some portion of photon energy is converted into the electron kinetic energy. At later times (~2 ps), the KETOF distribution stays unchanged, showing a double splitting and reaching $v_z = \pm 960$ m/s, the limit determined by the total available energy for the I channel.

Clearly, the transition is a parallel type and the I channel is dominant. If the PESs are similar to those of the alkyl iodides, the I channel results from the nonadiabatic interaction and this coupling is very strong. The high-velocity iodine atoms peak at 820 m/s, which corresponds to 73% of the available energy channeling into the translational energy and 27% into internal excitation of the phenyl radical. The KETOF profiles at long delay times are very similar to those observed by El-Sayed's group[76] using nanosecond lasers. With femtosecond lasers, we can see the KETOF evolution during the dissociation. The lower-velocity (≤550 m/s) iodine atoms appear later than the high-velocity (~800 m/s) ones. When the intensity of a certain portion of the I^+ KETOF distribution is monitored while the delay time is scanned, the dynamics of iodine atom formation

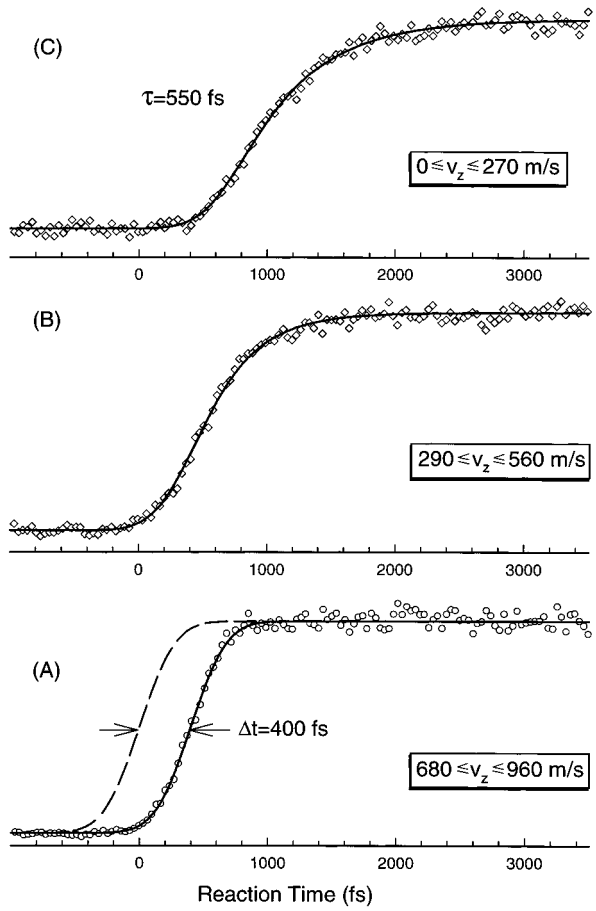

Figure 19. (A) Transient obtained by gating only the high-velocity ($680 \leq v_z \leq 960$ m/s) component of the I^+ KETOF distribution (iodobenzene dissociation). A 400-fs coherent shift from time zero is observed. The system response function (dashed line) is shown. Note that no ion-fragmentation signal was produced at this high velocity. (B, C) Transients obtained by collecting the medium- ($290 \leq v_z \leq 960$ m/s) and low- ($0 \leq v_z \leq 270$ m/s) velocity ion signal in the KETOF distribution. A small contribution from ion fragmentation around $t = 0$ has been subtracted from both transients. Note that the transient in (B) with the higher velocities appears earlier than the transient in (C) with the lower ones. The transient in (B) has a ~400-fs coherent shift from time zero, and the transient in (C) has a 550-fs rise (see the text for details).

with different kinetic energies can be separately observed in this fs−KETOF experiments.

When only the high-velocity ($700 \leq v_z \leq 960$ m/s) iodine signal is collected, the transient exhibits a very rapid rise with a coherent 400-fs shift (not growing) from the zero-of-time, as shown in Figure 19A. The contribution from the ion fragmentation at the earlier delay time was found to be negligible. The observation of the coherent delay is a manifestation of the wave-packet motion on the repulsive PES, as observed in I_2, ICN, and CH_3I, and establishes the assignment of the high-velocity component to the direct dissociation of the C−I bond through the (n, σ^*) excitation. The delay time therefore reflects the dynamics of the phenyl−iodine bond breakage on the (n, σ^*) potential surface.

When the medium ($290 \leq v_z \leq 560$ m/s) and low ($0 \leq v_z \leq 270$ m/s) velocities of iodine atoms in the I^+ KETOF distribution are monitored, the transients, after subtraction of the contributions from the ion fragmentation, are shown in parts B and C of Figure 19. The buildup of these transients is slow (not coherent), reaching their plateau values at about 1.3 and 2.2 ps, respectively. These features can also be seen in Figure 18

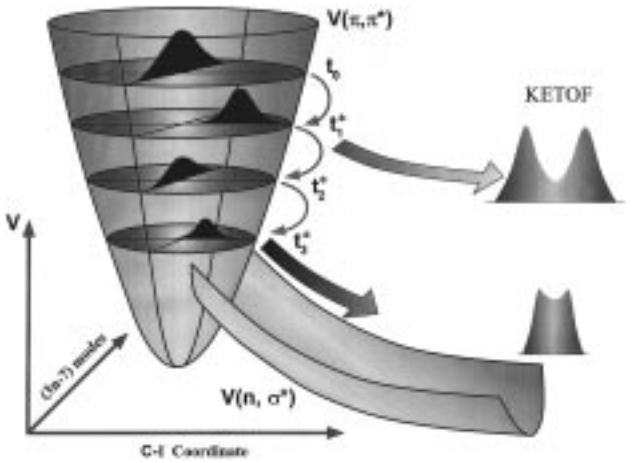

Figure 20. Schematic drawing of the excited bound- and repulsive-state PESs $V(\pi, \pi^*)$ and $V(\mathrm{n}, \sigma^*)$, respectively, illustrating the time−velocity correlation during dissociation in iodobenzene. At $t = 0$, a wave packet is created on the $V(\pi, \pi^*)$ surface by absorption of one pump photon. At $t_1^{\ddagger}$, enough energy flows into the C−I coordinate through IVR and the C−I bond is broken with high total available energy. The observed I^+ KETOF signal has a large-velocity distribution and high anisotropy. The C−I stretching motion can also couple with other bath modes ($t_2^{\ddagger}$). After a certain time, the energy flows back to the C−I coordinate and the C−I bond breaks with low total available energy ($t_3^{\ddagger}$). The resulting I^+ KETOF shows a small-velocity distribution and low anisotropy.

under careful examination. The medium-velocity iodine atoms appear earlier than the low-velocity ones. The transient (not shown) obtained by monitoring both the low- and medium-velocity components together exhibits a near-single-exponential buildup with a rise time of 550 fs and a delay time of ∼400 fs. These observations indicate that the low-velocity ($0 \leq v_z \leq$ 560 m/s) iodine atoms come from an indirect dissociation channel. The 550-fs rise time reflects the overall rate of the reaction starting from the phenyl-type modes and ending in final C−I fragmentation.

At our pump wavelength, excitation of the phenyl system is to the $^3(\pi, \pi^*)$ state, which has a significant oscillator strength because of the presence of the heavy iodine atoms. The optical excitation to the $^3(\pi, \pi^*)$ state at t_0 is not expected to deposit appreciable vibrational energy into the reaction coordinate, since the C−I bond is, in zeroth-order, nearly unaltered upon excitation. Figure 20 schematically illustrates this dynamical process. With this high vibronic energy in the $^3(\pi, \pi^*)$ phenyl ring modes, the wave packet spreads rapidly among vibrational modes and the C−I mode can quickly become activated at $t_1^{\ddagger}$ through IVR. This is then followed by a coupling to the repulsive (n, σ^*) surfaces, leading to the cleavage of the C−I bond. For a given total energy, the coupling strength between $V(\pi, \pi^*)$ and $V(\mathrm{n}, \sigma^*)$ determines the probability of this nonadiabatic transition. Theoretically, this can be treated as a Landau−Zener avoided crossing. If the initial IVR is complete, that is, the total energy is distributed among all vibrational modes, we can, in principle, calculate the dissociation rate by RRKM theory, combined with the nonadiabatic transition probability, and the observed transient describes two sequential processes determined by IVR and RRKM rates.

However, in our case, the observed 550-fs rise time is so fast that the initial IVR is expected to be incomplete, that is, a restricted process (the system has 30 vibrational modes, and RRKM rates would be relatively smaller). If the dissociation rate is comparable to the IVR rate, the activated C−I mode can also redistribute its energy to the surrounding bath modes of the phenyl system ($t_2^{\ddagger}$ in Figure 20). After a certain time, the energy flows back into the C−I coordinate ($t_3^{\ddagger}$) with less available energy for dissociation. Our experimental results are consistent with this dynamical picture. By detecting the final product of I atoms, we observed a time−velocity correlation for this indirect dissociation: the low-kinetic-energy iodine atoms build up more slowly than the medium-kinetic-energy ones, as shown in parts B and C of Figure 19. The 550-fs rise time reflects the overall rate from the restricted IVR and bond-breaking process. The ∼400-fs delay time is the minimum time for the C−I bond breakage even though enough energy has already been accumulated in the reaction coordinate of C−I, as observed in the direct dissociation of the C−I bond by $\sigma^* \leftarrow$ n excitation.

Besides the vibrational coherent motion depicted above, we have also considered the rotational motion of the parent molecules in relation to τ_{reac}, since the initial anisotropy created by the pump laser pulse can, in principle, be rapidly destroyed by rotational dephasing. Specifically, we performed experiments at two rotational temperatures, 10 and 300 K, and found that the transients do not show significant differences. Since the rotational coherence times (τ_c) differ by a factor of 5.5 for these two extreme temperatures,[53] these experimental observations suggest that rotational dephasing does not play a significant role. This is consistent with the fact that the dynamics involved here are faster than τ_c (τ_c(300 K) = 1.1 ps and τ_c(10 K) = 6.0 ps). However, it should be noted that if $\tau_{\mathrm{reac}} \geq \tau_c$, then the rotational dephasing has to be considered, especially for the initial dynamics.[53]

C. Two-Bonds Breakage: Sequential Processes. Here, we studied a reaction involving multiple-bond breakage by depositing enough energy into a system with two C−I bonds. The questions then are the following: What are the time scales and what is the mechanism, concerted or sequential? A typical system is that of a general class of halogen-atom elimination in many organic reactions.[77] The reaction we studied involves the following steps:

$$IF_2C{-}CF_2I + h\nu \rightarrow [I\cdots CF_2{-}CF_2I]^{*\ddagger} \rightarrow I^*/I + C_2F_4I^{\dagger} \quad (13a)$$

$$C_2F_4I^{\dagger} \rightarrow F_2C{=}CF_2 + I \quad (13b)$$

Previous studies of this reaction with picosecond resolution[66,78] revealed that this two-center elimination is a two-step, nonconcerted process involving the intermediate $C_2F_4I^{\dagger}$.

The time scales for the two bond fissions are 2 orders of magnitude different; the primary bond breakage, reaction 13a, takes several hundred femtoseconds (<500 fs), but the secondary elimination takes 30−70 ps depending on the excitation energy. The former is due to the direct repulsive (n, σ^*) excitation in the C−I bond, while the latter elimination, reaction 13b, is directly governed by the energy redistribution and the rate of bond breakage of $C_2F_4I^{\dagger}$. The PTS experiments[79] at 308 nm from Lee's group gave a ∼7.1 ± 2.5 kcal/mol barrier for the dissociation of the intermediate $C_2F_4I^{\dagger}$. Here, with femtosecond resolution and from measurements of the time evolution of products, the product−velocity distributions and the recoil anisotropy, the reaction dynamics and mechanism are microscopically elucidated.

The I^+ KETOF distributions for the parallel ($\chi = 0°$) and magic-angle ($\chi = 54.7°$) excitation are displayed in Figure 21 for 1- and 600-ps delay times. For the magic-angle KETOF shape at 1 ps, the velocity distribution is essentially flat, as

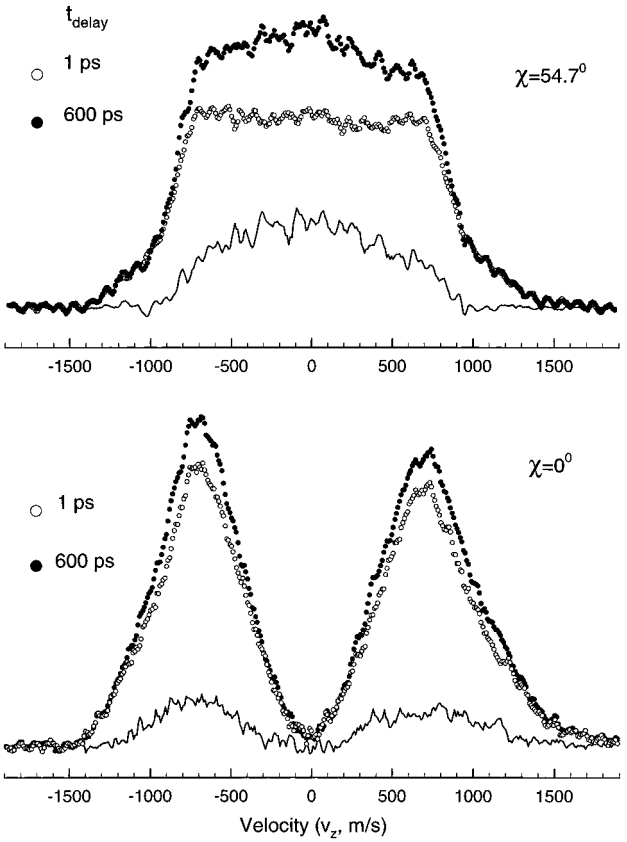

Figure 21. I^+ KETOF distributions (1,2-diiodotetrafluoroethane elimination reaction) for two typical delay times of 1 and 600 ps at $\chi = 54.7°$ (top) and $\chi = 0°$ (bottom). The difference of each of the two KETOF distributions (solid line) represents the contribution of the secondary iodine bond cleavage. The clear double peaks of the I^+ KETOF distributions at $\chi = 0°$ show a pure parallel transition with a very high anisotropy.

predicted by theory for a direct femtosecond dissociation, similar to those observed in I_2 and CH_3I. Indeed, this distribution reflects the primary C−I bond breakage. The earlier I^+ KETOF evolution of the first bond breakage around $t = 0$ is the same as that observed in I_2, ICN, and CH_3I, but here we focus on the difference between the first and second bond fission. At longer times, the distribution displays a buildup of intensity around $v_z \approx 0$, shown at 600 ps, reflecting the process of the secondary C−I elimination. The intensity difference for the two reaction times is also shown in Figure 21. A similar conclusion is reached for the $\chi = 0°$ results. To obtain the complete temporal behavior, we gated the slow-velocity portion of the distribution ($-250 \le v_z \le 250$ m/s) at the magic angle while varying the delay time. The biexponential rise of the femtosecond transient, shown in Figure 22, gives the two distinct reaction times for the two steps of C−I elimination: $\tau_1 \approx 200$ fs and $\tau_2 = 25$ ps, consistent with the behavior of the KETOF distributions.

From the magic-angle I^+ KETOF distribution, we obtained the laboratory recoil speed distribution of iodine atoms at 1-ps reaction time (Figure 23a). Two distributions, which peak at 850 and 1200 m/s, were obtained for the primary elimination, corresponding to the formation of the product in both spin−orbit states, I* and I. This is a characteristic of alkyl halide bond breakage with femtosecond dissociation times.[11] The large translational-energy release in such a short time excludes the possibility of breaking two C−I bonds concertedly. The excitation energy is 103 kcal/mol, and if two bonds ($\Delta H \approx 59$ kcal/mol for the I channel)[79] are involved, no such translational energy can be produced. This conclusion is entirely consistent

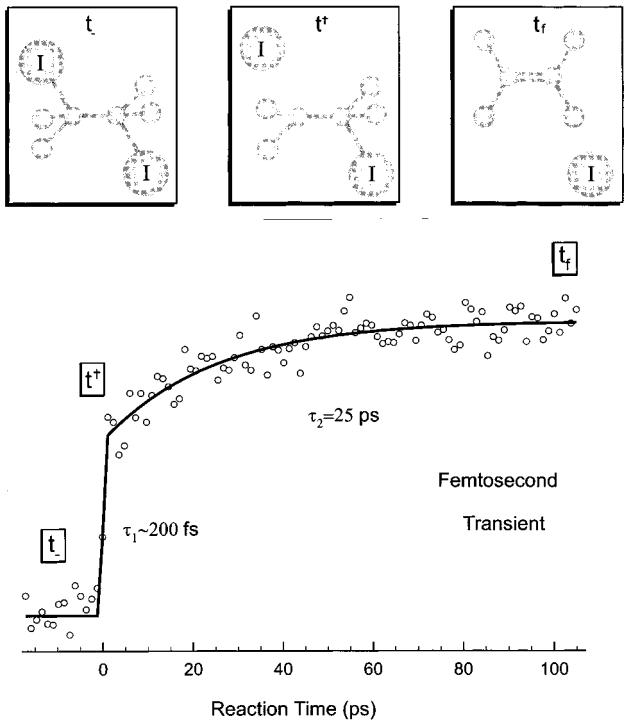

Figure 22. Transient obtained by gating the slow-velocity ($-250 \le v_z \le 250$ m/s) portion of the I^+ KETOF distribution at the magic angle as a function of the delay time ($C_2F_4I_2$ reaction). The slow-rise signal results from the secondary iodine bond breakage with a 25-ps lifetime, and the initial rapid rise is due to the primary iodine bond cleavage with a ~200-fs lifetime. Three structures are shown on the top to indicate the reaction: prior to the femtosecond excitation (t_-), after the primary bond breaking ($t^\dagger$), and when the final elimination (t_f) is reached.

with the biexponential transient behavior in Figure 22; the first "rise" (~200 fs) is due to the primary elimination. From measurements of the polarization dependence of the I^+ KETOF distribution (parallel vs magic angle), we also deduced the anisotropy parameter: $2.0 \le \beta \le 1.9$. The value is close to an ideal parallel transition ($\beta = 2.0$), that is, the transition moment is parallel to the C−I bond direction, and again is consistent with the observed prompt elimination process being caused by the repulsive force.

In the primary C−I breakage, we observe that the I* and I branching is 0.7 and 0.3, respectively. This branching is similar to that observed in the CH_3I.[11,55−57] The speed distributions do reach the limiting values determined by the total available energy for both I* and I channels (1100 m/s for I* and 1460 m/s for I). The average translational-energy release $\langle E_T \rangle / E_{avl}$ for each channel is found to be 59% for I* and 67% for I. Both translational-energy distributions are broad, and the full-width at half-maximum is 8.5 kcal/mol for I* and 19.5 kcal/mol for I. Theoretically, we predict that 86% of the available energy should appear as translation for a rigid radical (no vibrational excitation) following an impulsive bond breakage; for a "soft" radical, we obtained 13%.[80] Our experimental values are more toward the rigid-radical limit.

The secondary elimination dynamics have a different reaction time and velocity characteristic but surprisingly similar recoil anisotropy. After the femtosecond primary elimination, the observed 25-ps rise of the I atom (Figure 22) represents the time scale for energy redistribution to deposit enough energy in the reaction coordinate of the intermediate $[CF_2I-CF_2]^\dagger$ to break the second C−I bond. This is consistent with the previous picosecond studies and is further supported by the observation

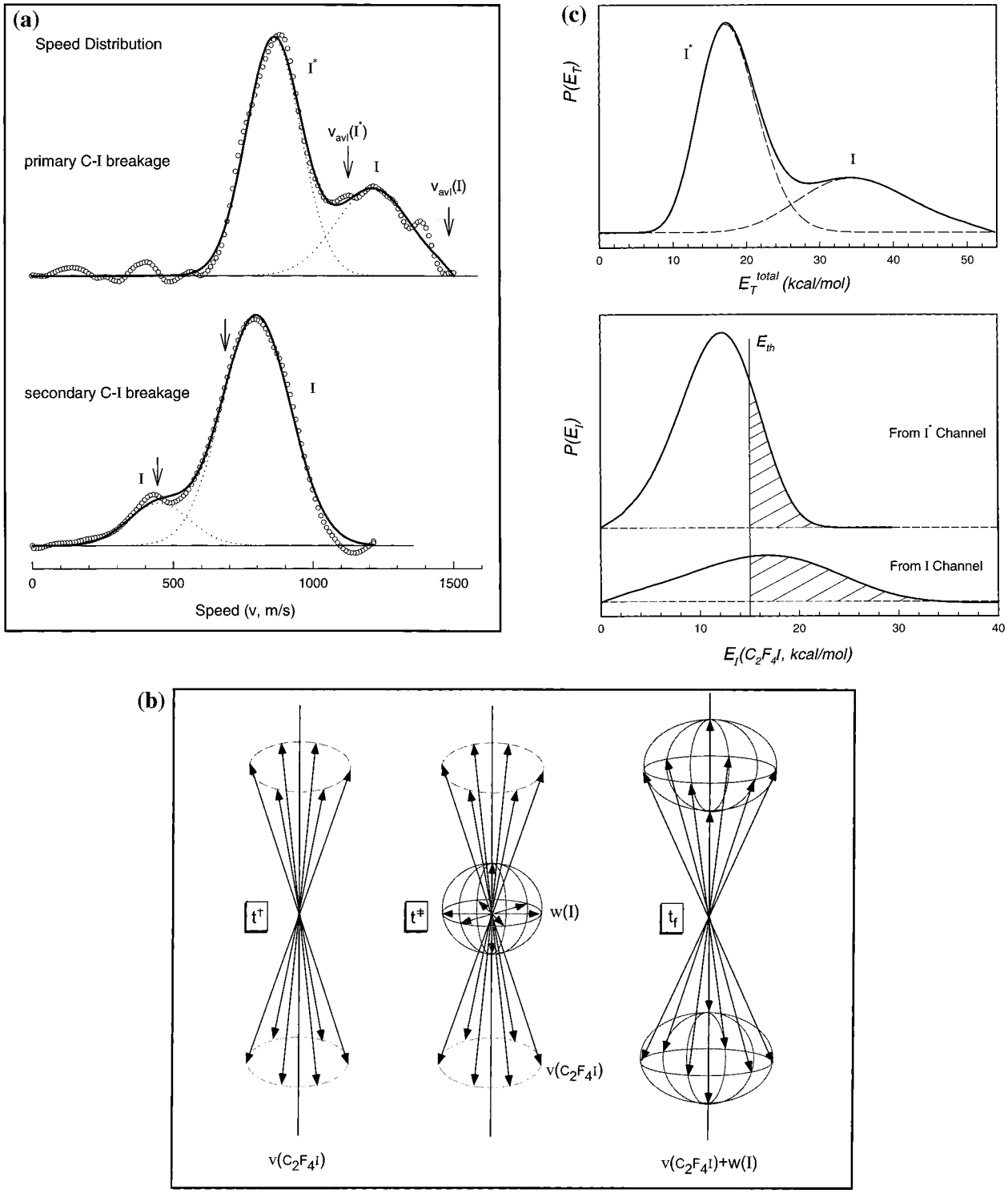

Figure 23. (a) Recoil speed distributions of iodine from the primary and secondary C−I bond breakage deduced (and smoothed) from the magic-angle I^+ KETOF signal for the 1- and 600-ps delay times, respectively ($C_2F_4I_2$ reaction). Both I and I* channels are present from the primary bond breakage and reach their speed limits. The second iodine C−I cleavage only produces the ground-state I atoms because of energetics. The two arrows in the secondary speed distribution (bottom) indicate the peak speeds of the dissociating C_2F_4I radicals produced from the I* and I channels. (b) Schematic representation of the velocity-distribution evolution during dissociation, illustrating the observed high anisotropy for the secondary iodine atom. At $t^\dagger$, the c.m. velocity (**v**) of the C_2F_4I radical is obtained from the impulsive primary C−I bond breakage. At $t^\ddagger$, the high-activated radical dissociates into C_2F_4 and I, producing a small, isotropic velocity distribution (**w**) for the secondary I atom in the c.m. frame. Finally (t_f), the observed laboratory velocity distribution for the secondary I atom is addition of the two velocities, **v** and **w**. Because **w** is very small compared with **v**, the final velocity observed is dominated by **v**. (c, upper panel) c.m. translational-energy distribution from the primary iodine bond breakage at 1-ps delay time. This is composed of two components from the I* and I channel. (c, lower panel) Internal-energy distributions of the C_2F_4I radicals resulting from the I* an I channels, obtained by subtraction of the c.m. translational energy from the total available energy. The deduced decomposition threshold is also indicated, and the C_2F_4I radicals with internal energy larger than E_{th} dissociate into C_2F_4 and I (see the text for details).

of the broad speed distribution of I atoms from the secondary elimination (Figure 23a).

The velocity distribution for I atoms from the secondary bond breakage ($\chi = 0°$ of Figure 21) shows a very high angular

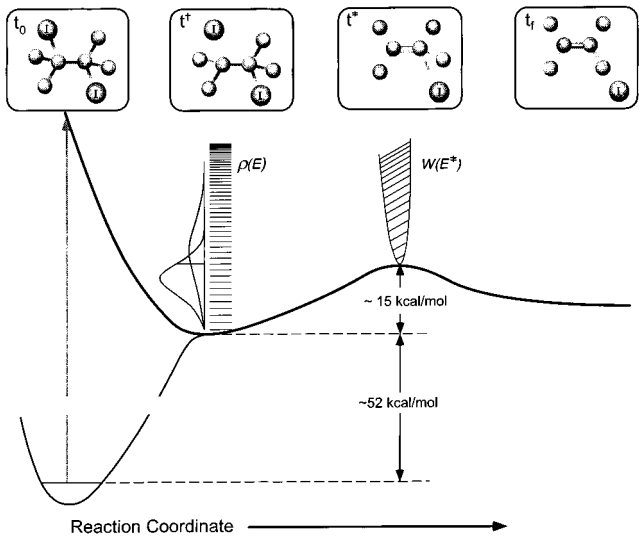

Figure 24. Schematic diagram of the reaction path for the two-iodine elimination from $C_2F_4I_2$. After the impulsive dissociation for the first C−I bond (t_0), the $C_2F_4I^\dagger$ is born at a special configuration with a broad vibrational excitation ($t^\dagger$). Some C_2F_4I radicals (∼35%) pass the decomposition barrier (∼15 kcal/mol) through a process of C−I stretching and C−C shrinking ($t^\ddagger$) to break the second C−I bond and make the C═C bond (t_f). The final products are two iodine atoms with difluoroethylene. The other (70%) radicals stay in the ground state. The corresponding structures at different stages are illustrated at the top.

anisotropy and the deduced anisotropy parameter (β) is ∼1.9, nearly the same as that for the primary bond breakage. Since the rotational time of the C_2F_4I intermediate is estimated to be between 2 and 8 ps, shorter than the observed 25-ps reaction time, the secondary elimination produces an isotropic, small speed distribution of I atoms. The addition of this small velocity to the large velocity of the c.m. of the C_2F_4I radical does not destroy the initial ($t = 0$) alignment; that is, the anisotropy of the secondary process "remembers" the primary elimination anisotropy and is determined mainly by the larger c.m. velocity of C_2F_4I (see Figure 23b). Thus, even though the measured anisotropy is very high, it does not reflect the long-lived state of the intermediate and it would have erroneously predicted a short-lived intermediate.

The c.m. translational-energy release for the first bond breakage and the resulting internal-energy distribution of the C_2F_4I intermediate obtained from conservation of energy are shown in Figure 23c. The $P(E_l)$ distributions are broad with peaks at 12 and 17 kcal/mol for the primary, I*, and I channels. When the I atom yield (Figure 21, $\chi = 54.7°$) from the secondary elimination is compared with the total primary iodine product, only ∼35% of the intermediate dissociates into C_2F_4 and I. From $P(E_l)$ vs E_l in Figure 23c, we therefore deduce an activation energy of ∼15 kcal/mol; the area under the distribution function of E greater than 15 kcal/mol is about 35% of the total one. This indicates that a small portion of $C_2F_4I^\dagger$ dissociates when it is created from the I* channel, while a large fraction decomposes if the I channel is involved; the secondary elimination only produces ground-state I atoms because of the energetics.

The deduced dissociation barrier (15 kcal/mol) is greater than the value, 7.1 ± 2.5 kcal/mol, reported from the PTS experiments.[79] The difference may be due to the difficulty in separating the I* and I channels, and the very broad I distribution at 308-nm excitation.[79] Moreover, the stimulated dissociation of the intermediate, which was observed in the PTS experiments, is negligible in our case because we did not observe the 475 or 670 m/s peaks in the speed distribution at 1 ps; these two values are the laboratory peak speeds of $C_2F_4I^\dagger$ from the I* and I channels, respectively, after the first bond breakage. The weakness of the second C−I bond is due to a concerted electronic path that breaks the C−I bond while forming a new C═C π bond, in contrast with the primary elimination, which only involves C−I cleavage. This weak C−I bond energy in the C_2F_4I radical can be estimated from D_0(C−I) − D_0(C═C) ≈ 8 kcal/mol.[81] With this ΔH value and the fact that I addition to C═C is endothermic, our value of the *effective* barrier (potential + centrifugal) is consistent with being larger than ∼8 kcal/mol.

Considering the decomposition threshold of ∼15 kcal/mol (see Figure 23c), the dissociating C_2F_4I radicals resulting from the primary I* and I channels have two peak speeds at 435 and 670 m/s (arrows in Figure 23a, bottom), respectively. The recoil speed distribution of the secondary I atoms shows two peaks at ∼435 and ∼800 m/s. These peak values of the C_2F_4I radical and the secondary I atom, resulting from the primary I* channel, are the same. This equality supports the previous description of the secondary elimination process. However, the values for the I channel differ by 130 m/s (800 vs 670 m/s). Besides the expected ∼670 m/s peak distribution for the secondary I atoms, it appears that a higher speed component (∼800 m/s) is part of the distribution that reflects a faster dissociation of the intermediate with higher internal energies, possibly in a nonthermal distribution.

After detachment of the I atom from $C_2F_4I_2$ in ∼200 fs, the C_2F_4I is born with high activation energy. Figure 24 illustrates the dynamical process along the reaction coordinate for this system. At t_0, a wave packet is initially excited on a repulsive surface V(n, σ^*). In about 200 fs, one of the C−I bonds is impulsively broken and the $C_2F_4I^\dagger$ is created in special distribution on a time scale shorter than that of vibrational motion(s), prior to IVR and reactivity. The femtosecond-activated, vibrationally hot $C_2F_4I^\dagger$ radical has a broad internal-energy distribution ($t^\dagger$). Two points should be emphasized here: (1) after the first impulsive C−I bond breaking, the internal energy is initially localized in the CF_2 side, not being distributed among all vibrational (rotational) modes in CF_2−CF_2I; (2) the IVR process may not follow the statistical behavior due to the initial special configuration of $C_2F_4I^\dagger$. This dynamical entry of the transition state is very critical to any nonstatistical behavior, as also observed in recent experiments involving dissociation of cyclic ketones.[82]

At the saddle point ($t^\ddagger$), the C−I bond stretches and the C−C bond shrinks. The dissociation barrier is determined by the concerted breakage of the σ(C−I) bond and the making of a π(C═C) bond. Given the ∼15 kcal/mol dissociation barrier and assuming the rotational excitation is inactive during dissociation, RRKM calculations of the radical-dissociation rate do give the picosecond time scale, but deviations still exist. So the initial IVR in $CF_2CF_2I^\dagger$ is not akin to complete thermal behavior on this ultrafast time scale, and this is consistent with the observation of the 800 m/s peak speed from the secondary iodine atoms (Figure 23a).

By employment of a femtosecond pulse to activate a reactive species through the breaking of one chemical bond or detachment of one atom in such a short time, the resulting internal energy may be localized in some vibrational states or bonds. The species is then made selectively at a special configuration.

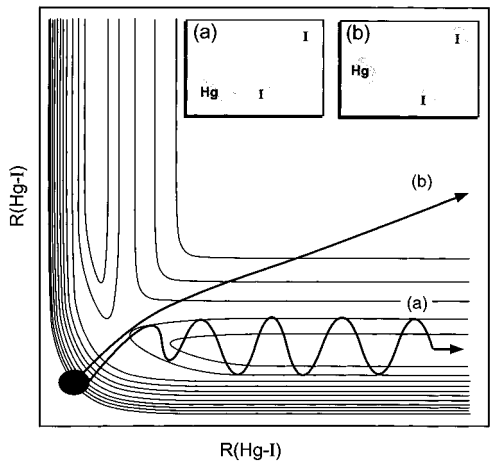

Figure 25. Schematic contour PES map at a linear configuration with two typical trajectories for the two-body and three-body dissociation. The wave packet is prepared on a steep repulsive wall right above the saddle point. The final products are shown in the two inserted panels.

This suggests some opportunities for investigating nonstatistical dynamics, including selective reactions even in the presence of IVR.[83]

D. Two-Bonds Breakage: Saddle-Point Transition States. In this section, we extend our studies to the case of ABA (IHgI) reactions, which define a saddle-point transition state. The dynamics involve two nuclear coordinates, symmetric and asymmetric stretches, besides the bend motion. The reaction is

$$\mathrm{IHgI} + h\nu \rightarrow [\mathrm{I}\cdots\mathrm{Hg}\cdots\mathrm{I}]^{*\ddagger} \rightarrow \mathrm{I}^*/\mathrm{I} + \mathrm{HgI(X)} \qquad (14a)$$

$$\rightarrow \mathrm{I}^*/\mathrm{I} + \mathrm{Hg} + \mathrm{I} \qquad (14b)$$

At 277-nm excitation, the complex involves the three types of motion on both the I* and I PESs: the asymmetric stretch, which leads to I*/I + HgI(X: v) formation; the symmetric stretch, which gives I*/I + Hg + I products; the bending motion of I−Hg−I, which is important for the rotational excitation of HgI(X: J) and for changing the molecular initial alignment (β).

The wave packet is prepared well above the saddle point and the three-body dissociation (I* + Hg + I) energy. Following the preparation, it spreads on the three-dimensional PES toward final products. The final outcome includes the reaction paths 14a and 14b, for both I* and I channels (see Figure 25). The energy distribution of I*/I is very broad, and the HgI(X: v, J) could be formed in all rovibrational levels extending to the dissociation limit.

From this laboratory, two femtosecond-resolved studies of HgI_2 dissociation in the gas phase have been reported before. One[84] focused on reaction 14a by monitoring the HgI formation using the LIF method. Coherent product formation and high rotational excitation of HgI(X: v, J) were observed and studied. In the same system, the solvation dynamics in solutions were also studied,[85] showing manifestations of vibrational relaxation and dephasing. The other study[12] involved the probing of the transition state by MPI and two-photon excitation dynamics. Reaction 14b has not been directly observed and studied.

Theoretically, classical and quantum calculations have been carried out by Gruebele et.al.,[86] using an empirical damped Morse potentials, to simulate the experimental findings. Recently, Burghardt and Gaspard[87] used the semiclassical methods of periodic-orbit quantization and equilibrium-point quantization to study the transition-state dynamics at the lower-energy regime. A series of resonances is characterized with regular classical dynamics. Near the saddle point, chaotic behavior was observed. Tannor and co-workers[88] proposed control of the branching of the two-body and three-body dissociation using sequences of optical pulses.

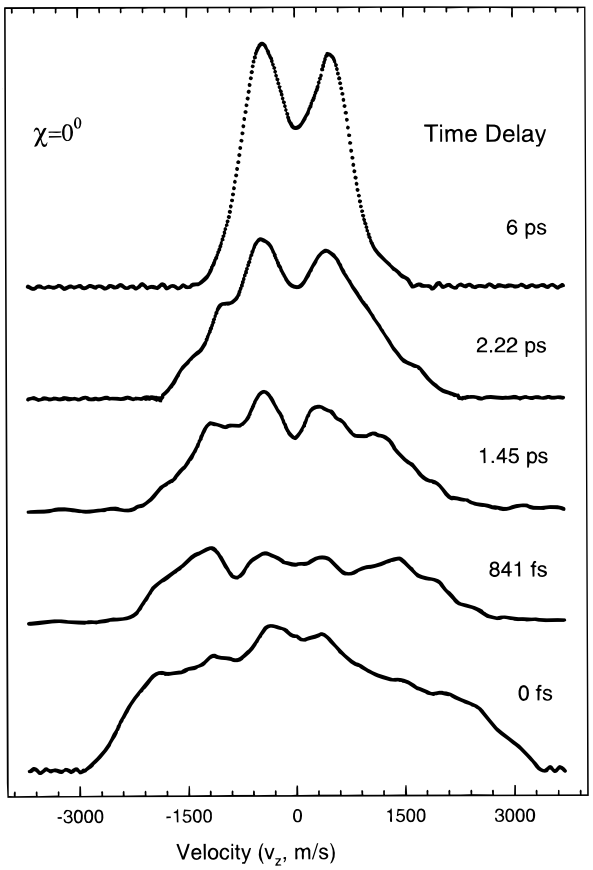

Figure 26. Femtosecond-resolved I^+ KETOF distributions from dissociation of IHgI at $\chi = 0°$. The signal at the early delay time is from excited $IHgI^+$ fragmentation, and the distribution stays unchanged after 6 ps. Note the dramatic change of the KETOF shape and the velocity-limit change with time.

Here, we report femtosecond studies of the dynamics of both the transition state and all iodine products. The results presented are all for one-photon excitation. This is done by carefully examining the power dependence of the initiating pulse. Figure 26 shows the time evolution of the I^+ KETOF distributions at $\chi = 0°$. The magic-angle data and the corresponding speed distributions are shown in Figure 27. For near-zero delay time, a very broad distribution is detected; it extends to about 2900 m/s. However, at 6-ps delay time, the distribution terminates at 1450 m/s with clear double peaks ($\chi = 0°$). No further change was found after 6 ps. At longer delay times, the signal from fragmentation of $IHgI^+$ decreases and the speed distribution narrows. This exactly reflects the time evolution of the transition state, as predicted in section III, for the case $E_{avl}{}^+(t_0) > E_{avl}(t_f)$. The probed ionic PESs may include both bound and repulsive states as evidenced by the earlier I^+ KETOF distribution at $\chi = 0°$. At long times, the wave packet spreads out on the global PES, and this results in a decrease of the signal. Also, at these times, the drop of both the neutral and ionic potential energy causes the narrowing of the speed distribution of I^+ cations.

The I^+ speed of 2900 m/s at $t = 0$ corresponds to 62314 cm^{-1} of total available energy relative to $I^+ + HgI$. By energy conservation, this value matches a four-photon probing. The three-photon probing gives a 1970 m/s speed limit for I^+ cations.

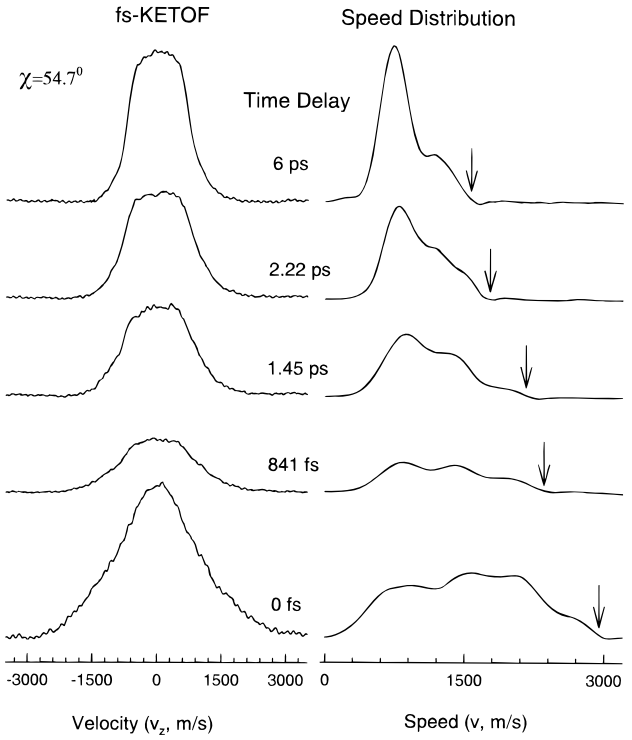

Figure 27. Femtosecond-resolved I^+ KETOF distributions at $\chi = 54.7°$ (IHgI reaction) shown on the left. The deduced speed distributions are on the right. Note the large change of the speed limits (shown by the arrows), which reflects the time evolution of the total available energy during dissociation, as discussed in section III.

The broad speed distribution can be understood because both three- and four-probe-photon ionization of $IHgI^{*‡}$ can access many ion states and produce I^+ cations with different amounts of available energy. From 0- to 841-fs delay time, the speed limit drops from 2900 to 2300 m/s while from 841 fs to 6 ps, the limit value only decreases by 800 m/s (see the arrows in Figure 27). This means that the transition-state species exhibits, at least, two different decay behaviors.

To obtain the complete temporal behavior, we gated the high-velocity portion of the I^+ distribution ($-2900 \le v_z \le -980$ m/s) at $\chi = 0°$ while varying the delay time. The result, shown in Figure 28A, does not show a single-exponential decay behavior. The femtosecond transient can be fitted to a biexponential decay with two distinct time constants: $\tau_1^‡ \approx 230$ fs and $\tau_2^‡ \approx 1.32$ ps, consistent with the observation of the KETOF evolution. We also measured the temporal behavior of Hg^+, which also results from fragmentation of excited $IHgI^+$ ($Hg^+ + I + I$). A similar transient was found with two time constants, $\tau_1^‡ \approx 200$ fs and $\tau_2^‡ \approx 1.44$ ps, as shown in Figure 28B.

The observed, first ~200-fs decay represents the time for the movement of the wave packet out of the initial Franck−Condon region. This rapid motion occurs because the packet experiences a strong repulsive force. Then it must pass the transition-state region near the saddle point and enters the valley of the products. Since both Hg and I are very heavy, ~200 fs is a reasonable time when compared with those of other systems: $I_2{}^{*‡}$ (65 fs), $ICN^{*‡}$ (70 fs), and $CH_3I^{*‡}$ (40 fs). After 200 fs, some portion of the wave packet evolves along the valley of the products I*/I + HgI(X) and the other makes an excursion to form I*/I + Hg + I. During this process, our probe pulses still can ionize these "loose" transition-state species, and overall, they live longer with a decay time constant of ~1.35 ps. This striking longer time of ~1.35 ps represents an average lifetime for all trajectories traveling through the transition-state region until the

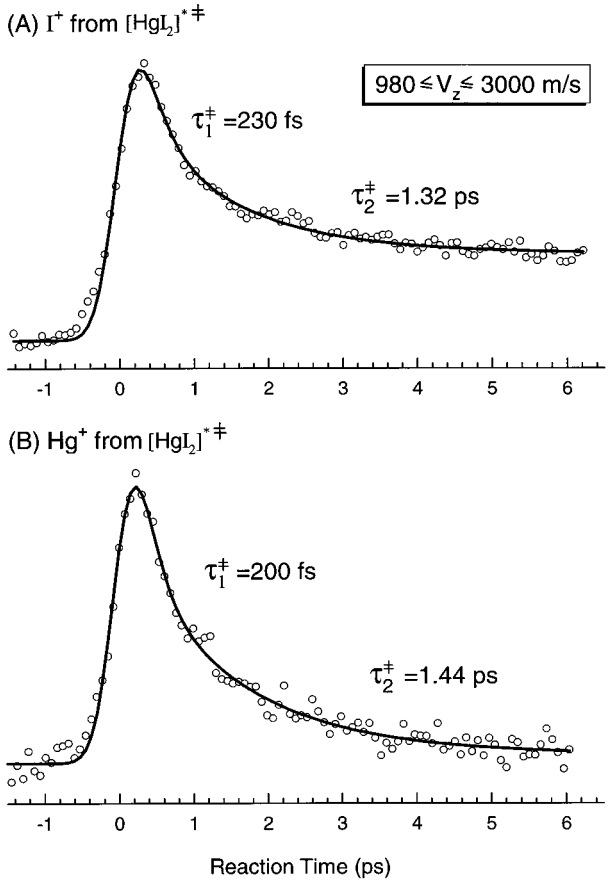

Figure 28. (A) Femtosecond transient obtained by gating the high-velocity component of the I^+ KETOF distribution at $\chi = 0°$ (IHgI reaction). The transient does not show a single-exponential decay behavior and can be fitted by a biexponential decay with two distinct time constants: $\tau_1^‡ = 230$ fs and $\tau_2^‡ = 230$ fs. (B) Femtosecond transient obtained from detecting the Hg^+ signal with a similar time behavior ($\tau_1^‡ = 200$ fs and $\tau_2^‡ = 1.44$ ps). Both (A) and (B) signals are from fragmentation of excited $IHgI^+$ and reflect the transition-state dynamics of $IHgI^{*‡}$.

completion of reactions 14a and 14b. This picture is further supported by the product-detection experiments, which are discussed below.

The I^+ KETOF distribution after 6 ps is unchanged and is sensitive to the probe wavelength. This indicates that the observed I^+ signal results from the neutral I-atom ionization. This also excludes the contribution from the HgI^{+*} fragmentation even though HgI is one of the products. The deduced speed distribution from the magic-angle data is shown in Figure 29. The speed distribution mainly consists of two components. One is from the reactions 14a and 14b for the I* channel, that is, forming I* + HgI(X) and I* + Hg + I. The ratio of the reactions 14a to 14b is close to 45%. The other involves the I channel giving I + Hg(X) and I + Hg + I as products. The ratio for these two reaction branches is less than 40%. The ratio for the two channels (I* and I) is about 4:1, which is less than the early reported value from the quantum-yield measurement (~13:1).[89]

If all the available energy (15 101 cm^{-1} above I + HgI(X)) is converted to translational motion, the observed speed distribution does indeed reach these limiting values (1000 m/s for I* + HgI(X) and 1430 m/s for I + HgI(X)). Figure 29 gives the starting speeds for the three-body dissociation: 796 m/s for I* + Hg + I and 1289 m/s for I + Hg + I, where the vibrational excitation of HgI(X: v) reaches the dissociation limit, ~2800 cm^{-1}. Considering the rotational excitation of HgI(X) (assum-

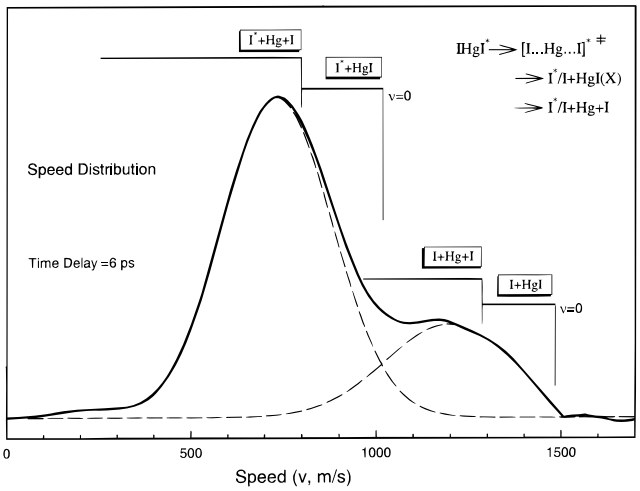

Figure 29. Speed distribution for the final neutral iodine atoms deduced from the I^+ KETOF distribution at $\chi = 54.7°$ for the 10-ps delay time (IHgI reaction). The recoil iodine speed distributions from the corresponding two-body and three-body dissociation for both I and I* channels are indicated. When the vibrational excitation energy of HgI (v) is equal to the dissociation limit, ~2800 cm^{-1}, the three-body dissociation begins.

ing $J = 150$ for the I* channel, $E_R = 634$ cm^{-1} and $J = 200$ for the I channel, $E_R = 1125$ cm^{-1}),[53] the speed values for I* and I shift to 740 and 1228 m/s, respectively. For the three-body dissociation, the translation-energy release to I*/I and I highly depends on the structure of the transition state. For example, assuming that the geometry of $IHgI^{*‡}$ is linear and that both Hg−I stretches receive the same translational-energy deposition, the I* and I would have the same final speed of 663 m/s from the I* + Hg + I channel. On the other hand, the speed would be 1075 m/s for the I and I coming from the I + Hg + I channel. If the $IHgI^{*‡}$ is bent by 80°, the speed is 502 m/s for the I* and I and 812 m/s for the 2I. In fact, by examining the speed distribution, one concludes that the two iodine atoms have different speeds and that the two symmetric stretches do obtain different energy during dissociation. This implies that the two Hg−I bonds take different times to break.

By performing the gating experiment of the I^+ velocity distribution ($0 \le v_z \le 980$ m/s) at $\chi = 0°$, we do observe the multiple-rise-time transient shown in Figure 30A. The transient exhibits a decay signal around $t = 0$. After 1 ps, the signal rapidly increases and then gradually grows to 6 ps. The transient was independently repeated many times, and the results are reproducible. The initial signal decay reflects the contribution from the transition-state population, and the later rise clearly results from neutral I atoms, consistent with the observed KETOF evolution. This rise signal, after subtraction of the transition-state contribution, is shown in Figure 30B. The transient is coherently shifted by 1 ps from $t = 0$ and increases rapidly at the beginning. Up to 2 ps, the signal reaches 70% of the asymptotic value. The 1-ps coherent shift is the shortest bond-breaking time for reactions 14a and 14b. After 2 ps, the transient gradually rises to 6 ps, which indicates that the bond-breaking time for the two Hg−I bonds ranges from 1 to 6 ps for reaction 14b. This rise signal at long times is *not* a kinetic behavior; instead, it represents superpositions of many coherent shifts of Hg−I bond breakage. The time scales will be further discussed after we present studies of the anisotropy in what follows. The anisotropy is directly relevant to the bending motion of I−Hg−I.

From simulation of the parallel I^+ KETOF distribution using the speed distribution deduced from the magic-angle KETOF

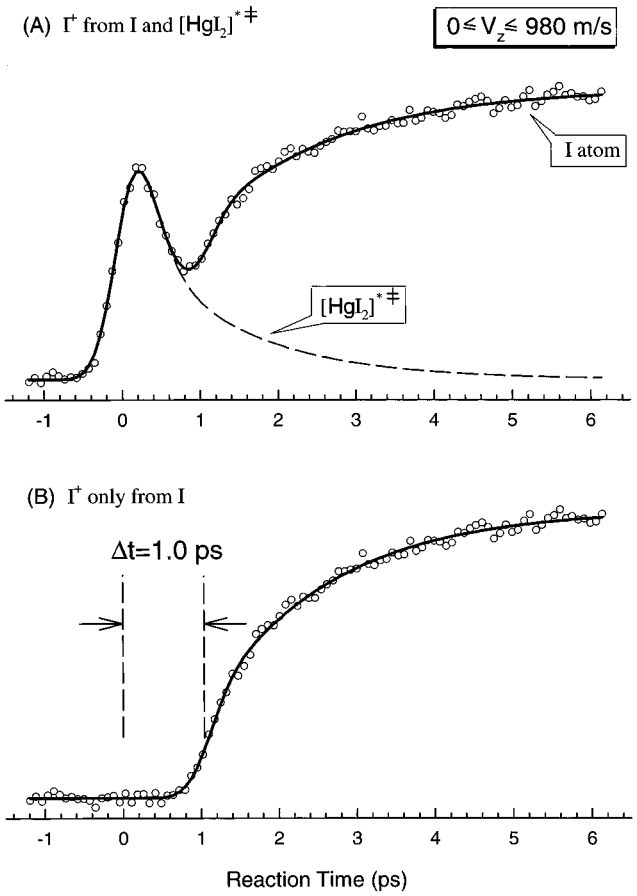

Figure 30. (A) Femtosecond transient taken by gating the slow-velocity component of the I^+ KETOF distribution at $\chi = 0°$ (IHgI reaction). The signal around $t = 0$ results from excited $IHgI^+$ fragmentation, which reflects the transition-state dynamics of $IHgI^{*‡}$, as observed in Figure 28. The delayed signal is from neutral iodine atoms. This transient was repeated many times and is reproducible. (B) Femtosecond transient obtained by subtracting the transition-state contribution from that in (A). This transient gives a coherent shift of 1 ps from time zero and increases rapidly at the beginning. Up to 2 ps, the signal reaches 70% of the asymptotic value and then gradually rises to 6 ps (see text).

data, we obtained an averaged anisotropy parameter $\beta \approx 0.5$ for the final iodine atoms. If we neglect the bending motion of IHgI in the ground state, the initial molecular geometry of IHgI is linear before the pump excitation. The relativistic ab initio calculations on $HgCl_2$ by Wadt[90] predict that the first excited state is bent by ~80°−120°. An analogous nonlinear geometry for the first excited state is also expected for HgI_2. Using magnetic circular dichroism, Mason[91] concluded that the initial absorption has Σ_u^+ and Π_u character due to the strong spin−orbital coupling, with a linear geometry description. This means that the initial excitation includes both parallel and perpendicular transitions. According to our study of χ dependencies, the excitation at 277 nm is a parallel transition. From the measured $\beta \approx 0.5$, we obtain a ~45° average angle of the final recoil velocity relative to the initial transition dipole. So after initial linear absorption of IHgI, and because of the anisotropic PES of the excited state, the molecule proceeds to a bending motion, together with the repulsive stretch motion. The bending motion results in the observations of the small value of the anisotropy of iodine atoms and the rotational excitation of HgI(X). Also, it enhances the interaction between I*/I and HgI(X) during dissociation.

The striking long bond-breaking time, ranging from 1 to 6 ps, can now be rationalized. First, the observed product-

formation time is consistent with the measured time scale of transition-state decay, and both are in the several-picosecond range. Second, since the terminal speed is small due to the heavy Hg and I atoms, the bond breakage takes longer time, as expected. Assuming that the I* atom is further moved by 6 Å from the equilibrium separation with Hg, for the reaction 14a, and that all available energy is converted to the translational motion, the terminal velocity is deduced to be 1330 m/s for I* + HgI(X: $\nu = 0$) and the minimum bond-breaking time is calculated to be ~450 fs. This time increases to 590 fs for the highest vibrational excitation of HgI(X: ν), that is, when the vibrational energy reaches the dissociation limit. Finally and importantly, the bending motion, together with the Hg−I stretching, increases the bond-breaking time owing to the enhancement of the interaction between I*/I and HgI(X).

Because the terminal speeds of I*/I + HgI(X), for low and high vibrational excitation of HgI(X: ν), are slightly different, the bond-breaking time for reaction 14a has an average dissociation time of ~1 ps. However, reaction 14b is different, and the relative velocity between each other highly depends on the geometry of the transition state. The total available energy (less than that for reaction 14a) needs to be divided into three atoms, and this division generally leads to small velocities. From the speed distribution (Figure 29), the speeds of the two iodine atoms from the three-body dissociation are different and this means that the deposition of the available energy into two Hg−I bonds is different. When less available energy is channeled into the second Hg−I bond, the relative velocity between Hg and I would be very small, although the lab velocity of the second I atom could be larger because of the addition of the c.m. velocity of Hg−I from the I−Hg bond breakage.

For example, assuming that the three-body dissociation of the I* channel proceeds with a linear geometry and that the total available energy (4696 cm^{-1}) channels 4175 cm^{-1} into the first I−Hg bond and 512 cm^{-1} into the second Hg−I bond, the observed lab velocities for the final products of I*, Hg, and I are 750, −136, and −535 m/s, respectively. The relative velocity between Hg and I is only 399 m/s. Therefore, it takes about 1.5 ps to break the second I−Hg bond for I to move 6 Å away from Hg, even without considering the bending motion. The bending motion (for $\nu = 1$, the period is ~1 ps) is on the time scale of the bond breakage and should also be included in the complete analysis of the HgI_2 dissociation on the three-dimensional PES. Molecular dynamics calculations are currently in progress in this laboratory.

E. Bond Breaking/Bond Making: Bimolecular Multiple Reaction Paths. We studied the bimolecular, charge-transfer (CT) reactions of 1:1 donor−acceptor complexes of benzene (and its deuterated and methyl-substituted species) with iodine,[8b] a benchmark system experimentally studied by Benesi and Hildebrand[92] and theoretically by Mulliken.[93] The reaction evolves on a multidimensional PES and has many pathways to the final products. It involves the following elementary steps:

$$Bz{\cdot}I_2 + h\nu \rightarrow$$

$$[Bz^+\cdots{}^-I_2]^{*\ddagger} \rightarrow Bz^+I^- + I \quad \text{(ionic channel)} \quad (15a)$$

$$\rightarrow Bz{\cdot}I + I^*/I \rightarrow Bz + I + I^*/I \quad \text{(neutral channel)} \quad (15b)$$

The transition state is directly reached by femtosecond excitation into the CT state of the complex, and the dynamics is followed by monitoring the product (I*/I) buildup or the initial transition-state decay. The ionic channel 15a produces a slow-velocity iodine atom (I) and the neutral channel 15b gives both fast (I*/I) and slow (I) iodine atoms. Therefore, different reaction pathways can be separately studied according to the iodine speed distributions.

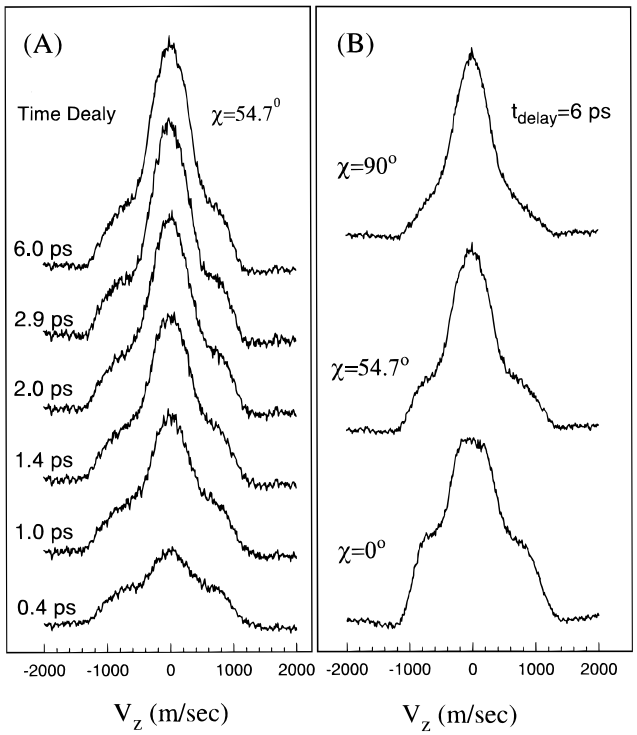

Figure 31. (A) Femtosecond-resolved I^+ KETOF distributions from the charge-transfer reaction of *o*-xylene with iodine at $\chi = 54.7°$. Two velocity distributions are clearly present. (B) χ dependencies of the I^+ KETOF distribution at a fixed delay time of 6 ps.

The femtosecond-resolved I^+ KETOF distributions at $\chi = 54.7°$ are shown in Figure 31A and the χ dependencies for a fixed delay time of 6 ps in Figure 31B, using the *o*-xylene·I_2 complex as an example. The signal shows two distributions, and both result from the neutral iodine atoms of the final products. At early reaction times, no I^+ signal was observed from transition-state *o*-xylene·I_2*‡ ionization fragmentation. After 6-ps delay time, the signal remains unchanged. The corresponding translational-energy distributions of iodine atoms, deduced from the magic-angle data in Figure 31A, are shown in Figure 32a. Clearly, these distributions exhibit two distinct components: one peaks at a low energy (less than 1000 cm^{-1}) and the other at a high energy of about 5000 cm^{-1}.

The dynamics of the different reaction pathways were selectively resolved by performing the gating experiments. The femtosecond transient, by collection of all I^+ signal, is shown at the top of Figure 32b. The signal could be fitted by a single-exponential rise with a 800-fs time constant. However, by gating the low- and the high-kinetic-energy portions in the I^+ KETOF distribution, two different temporal behaviors were observed. The femtosecond transients are shown at the bottom in Figure 32b. The high-energy component rises very rapidly (450 fs) and the low-energy one builds up much more slowly (1.4 ps). Considering the energy conservation, the high-energy iodine atoms results from reaction 15b, whereas the low-energy component includes both the slow iodine atoms from reactions 15a and 15b.

The recoil anisotropy was deduced for the two components by simulating the KETOF distribution at $\chi = 0°$ using the derived speed distribution (from the magic-angle data). By use of the Bz·I_2 complex as an example, the average anisotropy (β) of the high-energy component is ~1.0 and ~0.25 for the

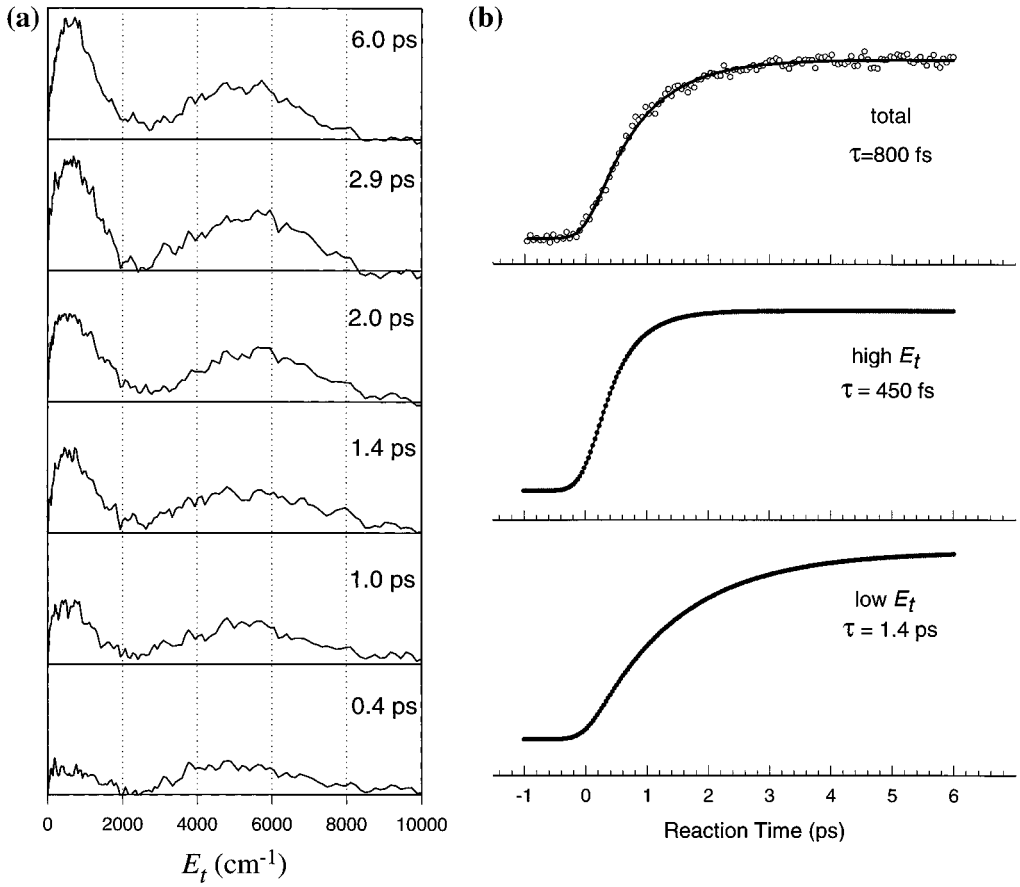

Figure 32. (a) Femtosecond-resolved translational-energy distributions of iodine atoms resulting from the *o*-xylene·I_2 reactions. These data are derived from the magic-angle KETOF distributions shown in Figure 31A. (b) Transients obtained from collecting the total iodine signal (top), and from gating at different kinetic-energy distributions (middle and bottom).

low-energy one. From the time-resolved experiments, the high-energy iodine atoms are produced in less than 450 fs. In such a prompt dissociation, the effect of rotational and vibrational motions is negligible, especially under our cold beam condition. Therefore, the β value ($\sim$1.0) suggests that the recoil direction is titled away from the transition dipole moment by an angle of $\sim$35°−40°, indicating that the transition-state structure is nearly axial, oblique.

We also monitored the transition-state decay of the 1:1 complexes. Two typical femtosecond transients from benzene·I_2 and mesitylene·I_2 complexes are shown in Figure 33a. The initial transition state decays extremely fast ($\sim$250 fs) and exhibits a biexponential behavior in the benzene·I_2 case. We have also varied the CT energy and studied the dynamics. By replacing the electron donor benzene by toluene, xylenes, and trimethylbenzenes, we also studied the effect of symmetry, geometry, and energetics (ionization potential minus electron affinity). Typical transients, by gating the total I^+ signal, are shown in Figure 33b for the various systems; the rise time ranges from 600 to 900 fs.

The elementary dynamics of these bimolecular CT reactions studied, which from above involve two exit channels, namely, the ionic and covalent pathways, give the following mechanistic picture. After femtosecond initiation of the CT, the prepared wave packet quickly moves on the CT surface and bifurcates near the ionic−neutral interaction region. Some portion of the population continues on the adiabatic, harpooning potential. The remaining, larger portion of the wave-packet population then quickly (250 fs) switches to the neutral repulsive surface through an intermolecular back electron transfer, leading to direct I + I*/I dissociation. The uncaged iodine atom dissociates freely and gives rise to the rapid (450 fs) high-translational-energy component. The caged iodine atom, on the other hand, encounters the electron-donor molecule and slowly escapes from its force field with significant loss in its translational energy. At the interaction region, a small portion of the wave-packet population transmits into the trapping well formed by the avoided crossing of the ionic and neutral surfaces. The trapped wave packet then slowly decays ($\sim$ 800 fs) by proceeding through the ionic exit or transmitting back to the lower neutral surface. MD simulations and descriptions of the HOMO/LUMO orbital interactions support our picture.[8b]

(F) Bond Breaking/Bond Making: Bimolecular Inelastic and Reactive Paths. We studied another bimolecular reaction that involves two pathways: an inelastic collision and a four-center reaction. The reaction is

$$CH_3I{\cdot}ICH_3 + h\nu \rightarrow CH_3 + [I{\cdot}ICH_3]^{\ddagger} \rightarrow CH_3 + I + CH_3I \quad \text{(inelastic collision)} \quad (16a)$$

$$\rightarrow [CH_3{\cdots}I{-}I{\cdots}CH_3]^{*\ddagger} \rightarrow 2CH_3 + I_2 \quad \text{(four-center reaction)} \quad (16b)$$

The dynamical process of inelastic collision 16a is illustrated in Figure 34a by the trajectory reflection. The translational hot I atom is formed in 125 fs by detaching the CH_3I group in direct dissociation of the moiety CH_3I (see section IV.A.3 for CH_3I dissociation). The reaction of CH_3I + I is observed from the van der Waals (vdW) geometry of the dimer at the I···I and C···I internuclear distances of the transition state. Depending on the translational energy of the I atom, the complex may be

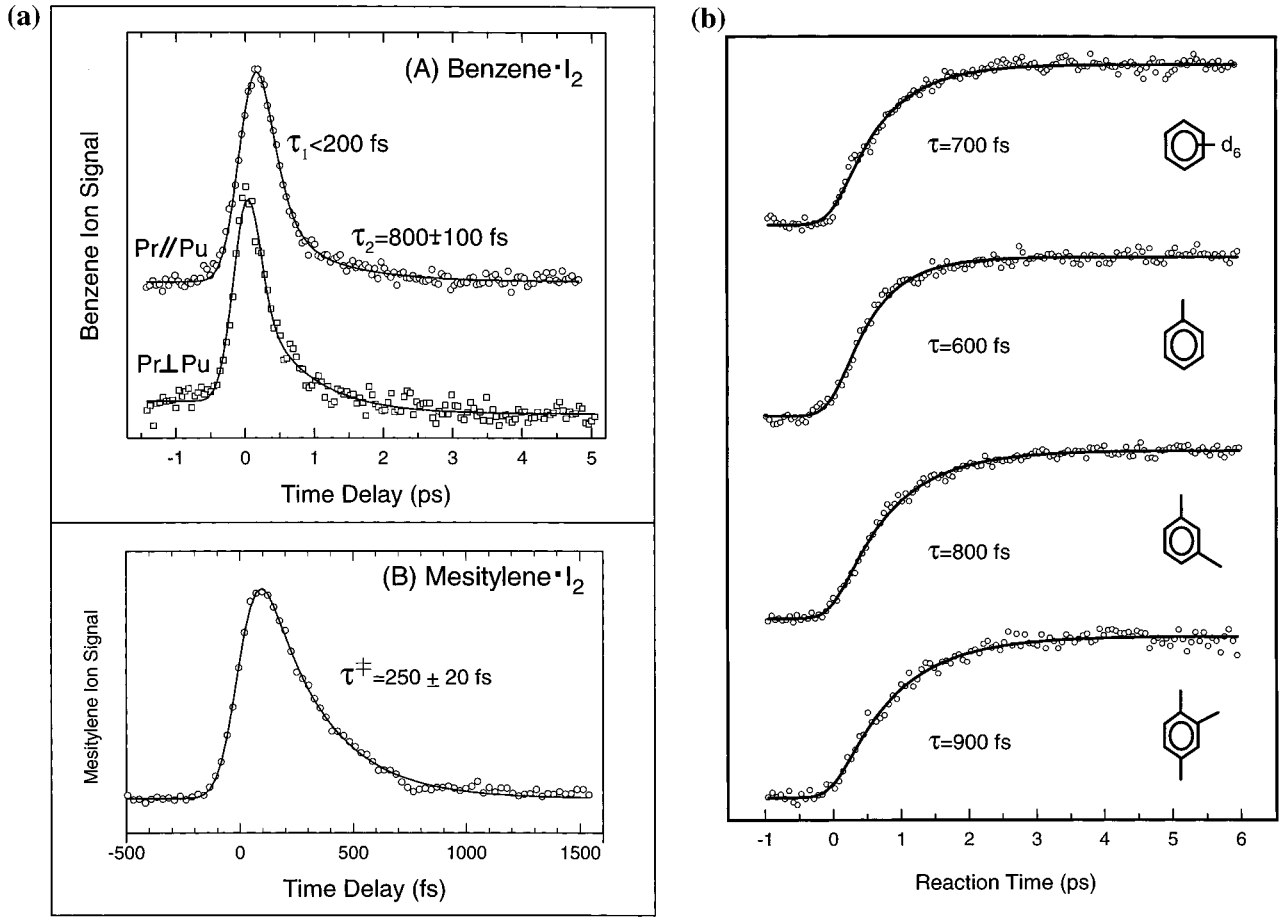

Figure 33. (a, A) Transients obtained by monitoring the signal in the Bz^+ mass channel as a function of the pump (277 nm) and probe (304 nm) delay time for the Bz·I_2 reaction. (a, B) Transient obtained on the mesitylene·I_2 reaction using the CPM laser system with 310 nm as the pump and 620 nm as the probe. (b) Typical iodine atom transients resulting from 277-nm excitation of the CT reactions of iodine with the substrate indicated. The electron donors for the transients shown here are, from top to bottom, deutrobenzene, toluene, *m*-xylene, and 1,2,4-trimethylbenzene. The apparent rise-time constants are indicated for each case.

trapped in the vdW potential well in the transition-state region, exchanges the energy between I and CH_3I, and finally decomposes into CH_3 and I. Thus, when the I atom buildup is monitored, the temporal behavior will reflect the nature of the transition state of the $CH_3II^‡$ complex. As with other real-time studies of bimolecular reactions,[8b,94,95] this approach allows for direct clocking of the complex with a limited impact parameter and relatively well-defined energy.

The I^+ KETOF distributions at $\chi = 0°$ for a fixed delay time of 10 ps are shown at the top in Figure 34b under monomer and dimer conditions. When the slow-velocity portion of the I^+ KETOF distribution (dimer) is gated and when the monomer contribution is subtracted, the transient, shown at the bottom in Figure 34b, exhibits a delayed, slow-rise behavior. The delay time is ~1.4 ps, and the rise time is ~1.7 ps. This transient was repeated many times and is very reproducible. The observed ~1.4-ps delay time is striking and indicates that a coherent wave-packet motion well persisted in the entrance channel during the inelastic collision between CH_3I and I.

For the minimum-energy dimer geometry calculated by Zeigler,[96] with reference to the crystal structure,[97] the I···I separation is estimated to be 3 Å and the structure is about 115° L-shaped with the two I atoms in proximity. The minimum-energy structure of the $CH_3II^‡$ complex is accordingly $CH_3I···I$ (the I−I distance is greater than 3 Å). Hence, the initial femtosecond pulse, which detaches the CH_3 group, suddenly turns the vdW attractive $CH_3I···ICH_3$ force into a repulsive interaction on the *ground-state* PES of $CH_3I + I$. The entire complex of $CH_3II^‡$ recoils away from the CH_3 group. In the complex, the velocity of the I atom relative to the CH_3I molecule is small with an upper limit of 400 m/s, which corresponds to a maximum of 1.29 kcal/mol of collision energy.

We have carried out preliminary MD simulations. Considering the large amplitude motion, a linear geometry was involved for simplicity. The $CH_3II^‡$ vdW ($CH_3I···I$) potential well is 1000 cm^{-1} deep, and the equilibrium distance is 3.5 Å. These MD simulations show that the I atom takes ~2 ps to separate from the CH_3I moiety with an 8-Å I−I distance. The c.m. of $CH_3II^‡$ moves ~5 Å, and because it has a velocity direction opposite from the I-atom (repulsive force) velocity direction in the complex, the entire inelastic process slows down.

The 1.7-ps rise time of I atoms directly measures the lifetime of the $CH_3II^‡$ complex trapped in the potential well (low v trajectories). It manifests any resonance motion in the $CH_3II^‡$ complex during the energy redistribution. Molecular-beam scattering experiments by Grice and by Ross[98] have shown a predominantly backscattered CH_3I from the reaction $CH_3 + I_2 \rightarrow CH_3I + I$ (at 2−3 kcal/mol collision energy), indicating a rebound repulsive release with the lifetime of the complex being comparable to or less than the rotational period. Our real-time results show the formation of a long-lived complex and indicate that the beam experiments were only sensitive to the short-lived, high-energy states of the complex. Syage's observed broad (I recoil) angular distribution is consistent with a long-lived complex.[63] The formation of a complex in the inelastic E → V process of HI + I (from HI dimers) has been shown recently

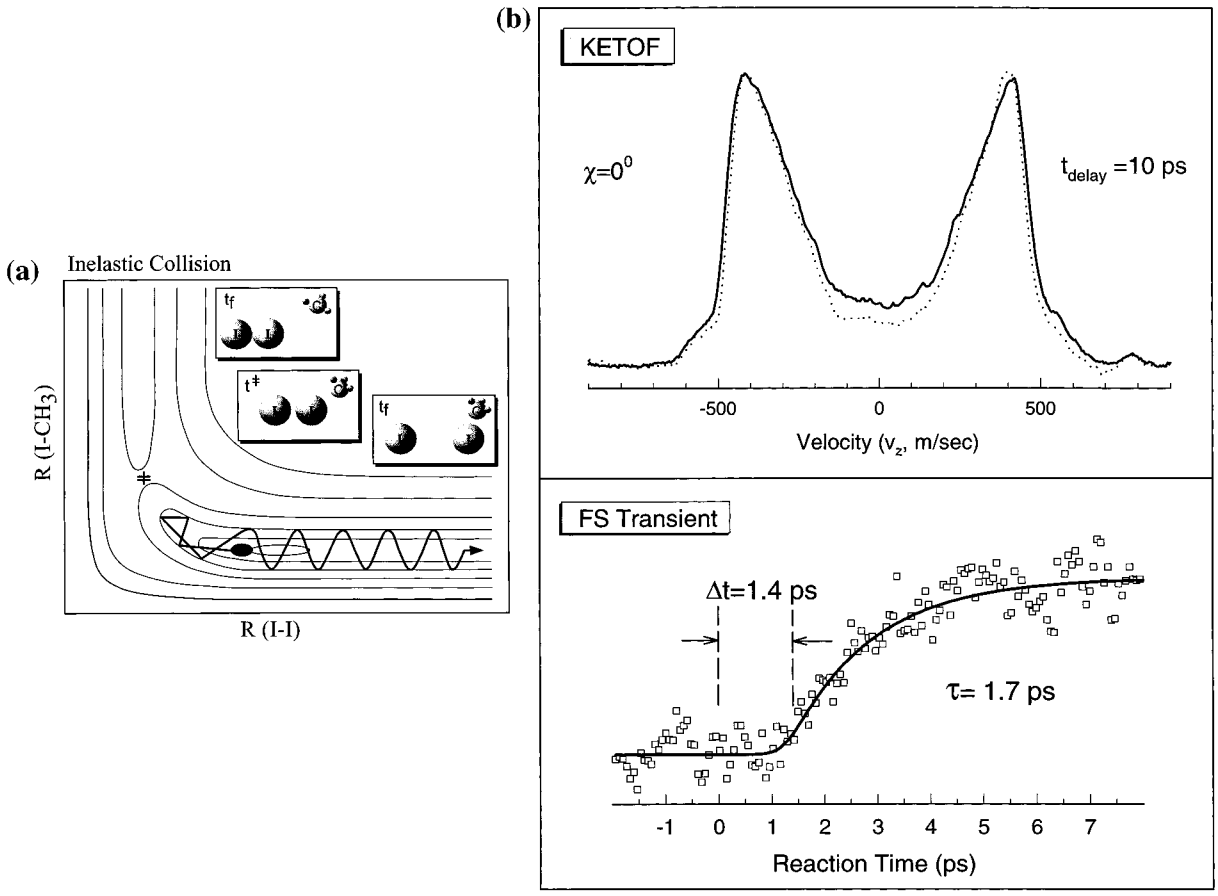

Figure 34. (a) Contour PES map for the full-collision, bimolecular $CH_3I + I$ reaction (schematic). An inelastic scattering trajectory is sketched. The corresponding structures during the reaction are shown in the three insets. (b, upper panel) I^+ KETOF distributions ($\chi = 0°$) obtained at a delay time of 10 ps under the monomer (dotted line) and the monomer/dimer conditions (solid line) for the bimolecular collision of CH_3I and I. (b, lower panel) Femtosecond transient after correction for the monomer contribution. The signal was best fitted by a delayed single-exponential rise (see text).

by detecting the translational-energy distributions of H atoms.[99] This is consistent with the above picture ($CH_3I + I$), and similar results were also obtained for $I + ICN$ in our studies of $(ICN)_2$. Recent MD calculations[100] have shown that the exothermic reaction of $CH_3 + I_2$ is favored in a near-collinear collision and occurs on a subpicosecond time scale (0.5−0.9 ps).

For the inelastic-collision dynamics described above, at the translational energy of our experiments, the wave packet cannot cross the barrier (~19 kcal/mol) to $CH_3 + I_2$ formation. By use of 304 nm as a pump, this reactive channel is still *not* open even for two-photon excitation, where the C−I bond breakage is still on the femtosecond time scale.[101] This is because the detached CH_3 takes up most of the available energy ($m_I E_{avl}/m_{CH_3I}$) either for the $I(^2P_{3/2})$ or $I(^2P_{1/2})$, as mentioned before. The reaction of $CH_3I + I(^2P_{3/2}) \rightarrow I_2 + CH_3$ is endothermic by 17.5 kcal/mol. (The channel of $CH_3I + I(^2P_{1/2})$, although it exceeds the endothermicity, is shown to proceed through the inelastic collision by $E \rightarrow V$ transfer to form $CH_3I(v) + I(^2P_{3/2})$.[102]) The fact that we do observe the I_2 formation under the dimer condition indicates a "four-center" mechanism. As shown in Figure 35, the transient, by gating the total I_2^+ signal, builds up very quickly, in less than 500 fs. With a 304-nm pump pulse (two photons), the I_2 molecule can be formed in the electronically excited B state and detected by a 1 + 1 REMPI process (277 nm). Indeed, the power dependence of the pump shows a quadratic behavior. No attempt yet was made to examine the ground-state I_2 formation, observed in one-photon A-band promotion.[103]

The key for the formation of I_2 is the cooperative nuclear motion of both C−I bonds in the four-center reaction 16b: a Bodenstein-type reaction.[104] Because the equilibrium distance of I_2 is 2.6 Å and the separation of I−I in the dimer is already about 3 Å, the I_2 molecule is formed promptly. Such I_2 formation has been studied in CW experiments[96,103,105] and with 10-ps resolution.[106] The femtosecond I_2 dynamics reported here can be rationalized using frontier orbitals. The initial femtosecond one-electron promotion makes the LUMO/HOMO interaction effective to create an I−I bond with the in-phase σ^* orbital ($n \rightarrow \sigma^*$ excitation) or s or p orbital (Rydberg excitation) combination on the two I atoms. Donaldson and co-workers[103] proposed a modified exciton model. After the excitation of a CH_3I moiety to the A continuum or to the Rydberg state, a partial charge transfer occurs from one I end to the other. This process results in some anion-type character with the C−I bond now experiencing a repulsive force.

The consequence of the orbital interactions is to form the I−I bond on the time scale of the C−I breakage (125 fs, since Rydberg excitation is similar[101]), consistent with the results in Figure 35 for I_2 production. The I_2 formation, which may be coherent, as shown in the case of molecular photodissociation CH_2I_2,[107] has also been observed in the photodissociation of the HI dimer[108,109] and again is a four-center reaction. Polanyi's group[110] observed the formation of Cl_2 and Br_2 by photoinitiating reactions of 2HX (X = Cl and Br) on LiF surfaces. This surface-aligned formation of X_2 is a four-center reaction.

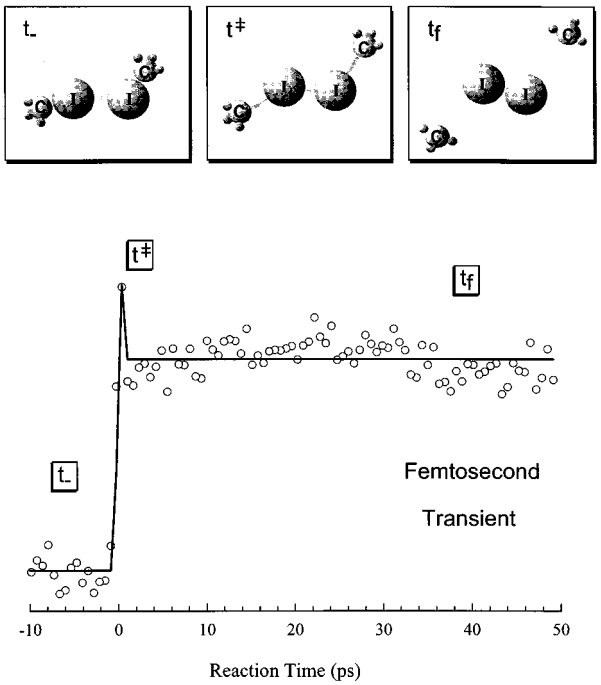

Figure 35. Femtosecond I_2^+ transient obtained under only the dimer condition $(CH_3I)_2$, detecting the I_2^+ mass signal. The corresponding reaction mechanism is sketched on the top by the structure changes during the reaction.

V. Conclusion

By resolving the femtosecond dynamics, together with the angular, state, and velocity distributions of reactions, we report studies of elementary steps in complex systems. The level of complexity varies from diatomics to polyatomics, from direct-mode to complex-mode, from one-center to two-center to four-center, and from unimolecular to bimolecular reactions. The systems examined here are of the following classes: (1) one-bond breakage, involving direct-mode reactions for iodine, cyanogen iodide, methyl iodide, and complex-mode reactions for iodobenzene; (2) two-bonds breakage, involving sequential processes for 1,2-diiodotetrafluoroethane and saddle-point transition states for mercury iodide; (3) bond breaking/bond making, involving bimolecular multiple reaction paths for benzene·I_2 complexes and inelastic and reactive paths for methyl iodide dimers.

When a complex reaction involves multiple pathways, from the transition state to final products, each pathway results in different energy partitioning among final products. For a given velocity range of a product, we can monitor the temporal evolution and then separately study each reaction path. Specifically, we have obtained (1) the temporal evolution of the transition state and the final products, (2) the time-resolved KETOF distributions, (3) the recoil anisotropy (β) in each channel, and (4) the state-resolved (I* and I) dynamics. A variety of dynamical behavior has been revealed, and these include product rotational and vibrational excitation, electronic and vibrational predissociation, saddle-point transition-state dynamics, intermolecular back electron transfer, and inelastic-collision and four-center reactions. Theoretical studies were also presented as part of the effort to compare with the experimental findings.

Acknowledgment. This work was supported by a grant from the National Science Foundation, the Airforce Office of Scientific Research, and the Office of Naval Research. We thank Dr. P. Y. Cheng for his effort and stimulating discussions, especially when experiments on the charge-transfer systems and iodobenzene were being conducted.

References and Notes

(1) *Femtosecond Chemistry*; Manz, J., Wöste, L., Eds.; VCH: Weinheim, 1995.

(2) *Femtochemistry: Ultrafast Chemical and Physical Processes in Molecular Systems*; Chergui, M., Ed.; World Scientific: Singapore, 1996.

(3) *Femtochemistry and Femtobiology*; Sundström, V., Ed.; World Scientific: Singapore, 1998.

(4) *Chemical Reactions and Their Control on the Femtosecond Time Scale, XXth Solvay Conference on Chemistry*; Gaspard, P., Burghard, I., Prigogine, I., Stuart, S. A., Eds.; Advances in Chemical Physics 101; John Wiley & Sons: New York, 1997.

(5) Zewail, A. H. *Femtochemistry: Ultrafast Dynamics of the Chemical Bond*; World Scientific: Singapore, 1994.

(6) Castleman, A. W., Jr.; Bowen, K. H., Jr. *J. Phys. Chem.* **1996**, *100*, 12911.

(7) Gerber, G. In *Chemical Reactions and Their Control on the Femtosecond Time Scale, XXth Solvay Conference on Chemistry*; Gaspard, P., Burghard, I., Prigogine, I., Stuart, S. A., Eds.; Advances in Chemical Physics 101; John Wiley & Sons: New York, 1997 and references therein.

(8) (a) Cheng, P. Y.; Zhong, D.; Zewail, A. H. *Chem. Phys. Lett.* **1995,** *237*, 399. (b) Cheng, P. Y.; Zhong, D.; Zewail, A. H. *J. Chem. Phys.* **1996,** *105*, 6216.

(9) Zewail, A. H. In *Femtochemistry and Femtobiology*; Sundström, V., Ed.; World Scientific: Singapore, 1998 and references therein.

(10) Kühlewind, H.; Kiermeier, A.; Neusser, H. J. *J. Chem. Phys.* **1986,** *85*, 4427.

(11) Zhong, D.; Cheng, P. Y.; Zewail, A. H. *J. Chem. Phys.* **1996,** *105*, 7864. Zhong, D.; Ahmad, S.; Zewail, A. H. *J. Am. Chem. Soc.* **1997,** *119*, 5978.

(12) Baumert, T.; Pedersen, S.; Zewail, A. H. *J. Phys. Chem.* **1993,** *97*, 12447. Pedersen, S.; Baumert, T.; Zewail, A. H. *J. Phys. Chem.* **1993,** *97*, 12460.

(13) Zhong, D.; Ahmad, S.; Cheng, P. Y.; Zewail, A. H. *J. Am. Chem. Soc.* **1997,** *119*, 2305.

(14) Cheng, P. Y.; Zhong, D.; Zewail, A. H. *Chem. Phys. Lett.* **1995,** *242*, 369. Cheng, P. Y.; Zhong, D.; Zewail, A. H. *J. Phys. Chem.* **1995**, *99*, 15733.

(15) Hall, G. E.; Sivakumar, N.; Ogorzalek, R.; Chawla, G.; Haerri, H. P.; Houston, P. L.; Burak, I.; Hepburn, J. W. *Faraday Discuss. Chem. Soc.* **1986,** *82*, 13.

(16) Hwang, H. J.; Griffiths, J.; El-Sayed, M. A. *Int. J. Mass Spectrom. Ion Processes* **1994,** *131*, 265

(17) Penn, S. M.; Hayden, C. C.; Muyskens, K. J. C.; Crim, F. F. *J. Chem. Phys.* **1988,** *89*, 2909.

(18) Mons, M.; Dimicoli, I. *J. Chem. Phys.* **1989,** *90*, 4037.

(19) Hertz, R. A.; Syage, J. A. *J. Chem. Phys.* **1994,** *100*, 9265.

(20) Simon, J. P. *J. Phys. Chem.* **1987**, *91*, 5378. Houston, P. L. *J. Phys. Chem.* **1987**, *91*, 5388. Hall, G. E.; Houston, P. L. *Annu. Rev. Phys. Chem.* **1989**, *40*, 375.

(21) Kinsey, J. L. *J. Chem. Phys.* **1977**, *66*, 2560.

(22) Dubs, M.; Brühlmann, U.; Huber, J. R. *J. Chem. Phys.* **1986**, *84*, 3106.

(23) Cline, J. I.; Taatjes, C. A.; Leone, S. R. *J. Chem. Phys.* **1990**, *93*, 6543.

(24) Syage, J. A. *J. Chem. Phys.* **1996**, *105*, 1007.

(25) Zare, R. N.; Herschbach, D. R. *Proc. IEEE* **1963**, *51*, 173.

(26) Dantus, M.; Rosker, M. J.; Zewail, A. H. *J. Chem. Phys.* **1987,** *87*, 2395. Rosker, M. J.; Dantus, M.; Zewail, A. H. *J. Chem. Phys.* **1988**, *89*, 6113. Dantus, M.; Rosker, M. J.; Zewail, A. H. *J. Chem. Phys.* **1988**, *89*, 6128.

(27) Greenblatt, B. J.; Zanni, M. T.; Neumark, D. M. *Chem. Phys. Lett.* **1996**, *258*, 523. Greenblatt, B. J.; Zanni, M. T.; Neumark, D. M. *Science* **1997,** *276*, 1675.

(28) Busch, G. E.; Mahoney, R. T.; Wilson, K. R. *J. Chem. Phys.* **1969**, *51*, 837.

(29) Mulliken, R. *J. Chem. Phys.* **1971**, *55*, 288. Tellinghuisen, J. *J. Chem. Phys.* **1973**, *58*, 2821.

(30) Williams, S. O.; Imre, D. *J. Phys. Chem.* **1988**, *92*, 6648.

(31) Roberts, G.; Zewail, A. H. *J. Phys. Chem.* **1991**, *95*, 7973; **1995**, *99*, 2520.

(32) Ling, J. H.; Wilson, K. R. *J. Chem. Phys.* **1975,** *63*, 101.

(33) Sabety-Dzvonik, M. J.; Cody, R. J. *J. Chem. Phys.* **1977**, *66*, 125. Baronavski, A. P.; McDonald, J. R. *Chem. Phys. Lett.* **1977**, *45*, 172.

(34) Marinelli, W. J.; Sivakumar, N.; Houston, P. L. *J. Phys. Chem.* **1984**, *88*, 6685. Hall, G. E.; Sivakumar, N.; Houston, P. L. *J. Chem. Phys.* **1986**, *84*, 2120.

(35) Nadler, I.; Mahgerefteh, M.; Reisler, H.; Wittig, C. *J. Chem. Phys.* **1985**, *82*, 3885.
(36) Hess, W. P.; Leone, S. R. *J. Chem. Phys.* **1987**, *86*, 3773.
(37) (a) O'Halloran, M. A.; Joswig, H.; Zare, R. N. *J. Chem. Phys.* **1987**, *87*, 303. Black, J. F.; Waldeck, J. R.; Zare, R. N. *J. Chem. Phys.* **1990**, *92*, 3519. Black, J. F. *J. Chem. Phys.* **1993**, *98*, 6853. (b) North, S. W.; Mueller, J.; Hall, G. E. *Chem. Phys. Lett.* **1997**, *276*, 103.
(38) Kash, P. W.; Butler, L. J. *J. Chem. Phys.* **1992**, *96*, 8923.
(39) Griffiths, J.; El-Sayed, M. A. *J. Chem. Phys.* **1994**, *100*, 4910.
(40) Goldfield, E. M.; Houston, P. L.; Ezra, G. S. *J. Chem. Phys.* **1986**, *84*, 3120.
(41) Guo, H.; Schatz, G. C. *J. Chem. Phys.* **1990**, *92*, 1634. Liu, L.; Fang, J.; Guo, H. *J. Chem. Phys.* **1995**, *102*, 2404.
(42) Coalson, R. D.; Karplus, M. *J. Chem. Phys.* **1990**, *93*, 3919.
(43) Williams, C. J.; Qian, J.; Tannor, D. J. *Chem. Phys.* **1991**, *95*, 1721. Qian, J.; Williams, C. J.; Tannor, D. J. *Chem. Phys.* **1992**, *97*, 6300.
(44) Lee, S. Y. *J. Chem. Phys.* **1992**, *97*, 227.
(45) Beswick, J. A.; Glass-Maujean, M.; Roncero, O. *J. Chem. Phys.* **1992**, *96*, 7514.
(46) Baer, M.; Kosloff, R. *Chem. Phys. Lett.* **1992**, *200*, 183.
(47) Yabushita, S.; Morokuma, K. *Chem. Phys. Lett.* **1990**, *175*, 518. Amatatsu, Y.; Yabushita, S.; Morokuma, K. *J. Chem. Phys.* **1994**, *100*, 4894.
(48) Wang, Y.; Qian, C. X. W. *J. Chem. Phys.* **1994**, *100*, 2707.
(49) Qian, J.; Tannor, D. J.; Amatatsu, Y.; Morokuma, K. *J. Chem. Phys.* **1994**, *101*, 9597.
(50) Bowman, J. M.; Mayrhofer, R. C.; Amatatsu, Y. *J. Chem. Phys.* **1994**, *101*, 9469.
(51) Wei, H.; Carrington, T., Jr. *J. Chem. Phys.* **1996**, *105*, 141.
(52) Wang, Y.; Qian, C. X. W. *Chem. Phys. Lett.* **1994**, *219*, 389.
(53) Zewail, A. H. *J. Chem. Soc., Faraday Trans. 2* **1989**, *85*, 1221. *Faraday Discuss. Chem. Soc.* **1991**, *91*, 207. Baskin, J. S.; Zewail, A. H. *J. Phys. Chem.* **1994**, *98*, 3337.
(54) Imre, D. G.; Kinsey, J. L.; Field, R. W.; Katayama, D. H. *J. Phys. Chem.* **1982**, *86*, 2564. Imre, D.; Kinsey, J. L.; Sinha, A.; Krenos, J. *J. Phys. Chem.* **1984**, *88*, 3956. Johnson, B. R.; Kittrell, C.; Kelly, P. B.; Kinsey, J. L. *J. Phys. Chem.* **1996**, *100*, 7743.
(55) Sparks, R. K.; Shobatake, K.; Carlson, L. R.; Lee, Y. T. *J. Chem. Phys.* **1980**, *75*, 3838.
(56) Baughcum, S. L.; Leone, S. R. *J. Chem. Phys.* **1980**, *72*, 6531. Hermann, H. W.; Leone, S. R. *J. Chem. Phys.* **1982**, *76*, 4766.
(57) Barry, M. D.; Gorry, P. A. *Mol. Phys.* **1984**, *52*, 461. van Veen, G. N. A.; Baller, T.; van Veen, N. J. A. *Chem. Phys.* **1984**, *87*, 405.
(58) Loo, R. O.; Hall, G. H.; Haerri, H. P.; Houston, P. L. *J. Phys. Chem.* **1988**, *92*, 5. Penn, S. M.; Hayden, C. C.; Muyskens, K. J. C.; Crim, F. F. *J. Chem. Phys.* **1988**, *89*, 2909.
(59) Chandler, D. W.; Janssen, M. H. M.; Stolte, S.; Strickland, R. N.; Thoman, J. W., Jr.; Parker, D. H. *J. Phys. Chem.* **1990**, *94*, 4839. Janssen, M. H. M.; Parker, D. H.; Sitz, G. O.; Stolte, S.; Chandler, D. W. *J. Phys. Chem.* **1991**, *95*, 8007.
(60) Lao, K. Q.; Person, M. D.; Xayariboun, P.; Butler, J. L. *J. Chem. Phys.* **1990**, *92*, 823.
(61) Hall, G. E.; Sears, T. J.; Frye, J. M. *J. Chem. Phys.* **1989**, *90*, 6234. Suzuki, T.; Kanamori, H.; Hirota, E. J. *J. Chem. Phys.* **1991**, *94*, 6607.
(62) Zhu, Y. F.; Grant, E. R. *J. Phys. Chem.* **1993**, *97*, 9582. Strobel, A.; Fischer, I.; Lochschmidt, A.; Müller-Dethlefs, K.; Bondybey, V. E. *J. Phys. Chem.* **1994**, *98*, 2024.
(63) Syage, J. A. *Chem. Phys.* **1996**, *207*, 411.
(64) Ohoyama, H.; Ogawa, T.; Makita, H.; Kasai, T.; Kuwata, K. *J. Phys. Chem.* **1996**, *100*, 4729.
(65) Dzvonik, M. K.; Yang, S.; Bersohn, R. *J. Chem. Phys.* **1974**, *61*, 4408.
(66) Knee, J. L.; Khundkar, L. R.; Zewail, A. H. *J. Chem. Phys.* **1985**, *83*, 1996.
(67) Shapiro, M.; Bersohn, R. *J. Chem. Phys.* **1980**, *73*, 3810. Kanfer, S.; Shapiro, M. *J. Phys. Chem.* **1984**, *88*, 3644. Shapiro, M. *J. Phys. Chem.* **1986**, *90*, 3644.
(68) Sundberg, R. L.; Imre, D.; Hale, M. O.; Kinsey, J. L.; Coalson, R. D. *J. Phys. Chem.* **1986**, *90*, 5001.
(69) Guo, H.; Schatz, G. C. *J. Chem. Phys.* **1990**, *93*, 393. Guo, H.; Lao, K. Q.; Schatz, G. C.; Hammerich, A. D. *J. Chem. Phys.* **1991**, *94*, 6562.
(70) Amatatsu, Y.; Morokuma, K.; Yabushita, S. *J. Chem. Phys.* **1991**, *94*, 4858.
(71) Amatatsu, Y.; Yabushita, S.; Morokuma, K. *J. Chem. Phys.* **1996**, *104*, 9783.
(72) Guo, H.; Schatz, G. C. *J. Phys. Chem.* **1991**, *95*, 3091. Guo, H. *J. Phys. Chem.* **1992**, *96*, 6629.
(73) Hammerich, A. D.; Manthe, U.; Kosloff, K.; Meyer, H.; Cederbaum, L. S. *J. Chem. Phys.* **1994**, *101*, 5623.
(74) O'Brien, S. C.; Kittrell, C.; Kinsey, J. L.; Johnson, B. R. *J. Chem. Phys.* **1992**, *96*, 67.
(75) Freedman, A.; Yang, S. C.; Kawasaki, M.; Bersohn, R. *J. Chem. Phys.* **1980**, *72*, 1028.
(76) Hwang, H. J.; El-Sayed, M. A. *J. Chem. Phys.* **1992**, *96*, 856. Freitas, J. E.; Hwang, H. J.; El-Sayed, M. A. *J. Phys. Chem.* **1994**, *98*, 3322, 12481.
(77) Lowry, T. H.; Richardson, K. S. *Mechanism and Theory in Organic Chemistry*, 3rd ed.; Harper & Row: New York, 1987.
(78) Khundkar, L. R.; Zewail, A. H. *J. Chem. Phys.* **1990**, *92*, 231.
(79) Nathanson, G. M.; Minton, T. K.; Shane, S. F.; Lee, Y. T. *J. Chem. Phys.* **1989**, *90*, 6157.
(80) Busch, G. E.; Wilson, K. R. *J. Chem. Phys.* **1972**, *56*, 3626, 3638.
(81) Carter, E. A.; Goddard, W. A. *J. Am. Chem. Soc.* **1988**, *110*, 4077.
(82) Diau, E. W. G.; Herek, J. L.; Kim, Z. H.; Zewail, A. H. *Science* **1998**, *279*, 847.
(83) Zewail, A. H. *Phys. Today* **1980**, *33*, 27 and references therein.
(84) Dantus, M.; Bowman, R. M.; Gruebele, M.; Zewail, A. H. *J. Chem. Phys.* **1989**, *91*, 7437.
(85) Pugliano, N.; Szarka, A. Z.; Hochstrasser, R. M. *J. Chem. Phys.* **1996**, *104*, 5062. Volk, M.; Gnanakaran, S.; Gooding, E.; Kholodenko, Y.; Pugliano, N.; Hochstrasser, R. M. *J. Phys. Chem. A* **1997**, *101*, 638.
(86) Gruebele, M.; Roberts, G.; Zewail, A. H. *Philos. Trans R. Soc. London A* **1990**, *332*, 223.
(87) Burghardt, I.; Gaspard, P. *J. Chem. Phys.* **1994**, *100*, 6395. Burghardt, I.; Gaspard, P. *J. Phys. Chem.* **1995**, *99*, 2732. Also in ref 4.
(88) Somlói, J.; Tannor, D. J. *J. Phys. Chem.* **1995**, *99*, 2552.
(89) Hofmann, H.; Leone, S. R. *J. Chem. Phys.* **1978**, *69*, 3819.
(90) Wadt, W. R. *J. Chem. Phys.* **1980**, *72*, 2469.
(91) Savas, M. M.; Mason, W. R. *Inorg. Chem.* **1988**, *27*, 658.
(92) Benesi, H. A.; Hildebrand, J. H. *J. Am. Chem. Soc.* **1949**, *71*, 2703.
(93) Mulliken, R. S. *J. Am. Chem. Soc.* **1950**, *72*, 610; **1952**, *74*, 811. Mulliken, R. S.; Person, W. B. *Molecular Complexes: A Lecture and Reprint Volume*; Wiley-Interscience: New York, 1969.
(94) Scherer, N. F.; Khundkar, L. R.; Bernstein, R. B.; Zewail A. H. *J. Chem. Phys.* **1987**, *87*, 1451; **1990**, *92*, 5239. Sims, I. R.; Gruebele, M.; Potter, E. D.; Zewail, A. H. *J. Chem. Phys.* **1992**, *97*, 4127.
(95) Ionov, S. I.; Brucker, G. A.; Jaques, C.; Valachovic, L.; Wittig, C. *J. Chem. Phys.* **1993**, *99*, 6553.
(96) Wang, P. G.; Zhang, Y. P.; Ruggles, C. J.; Ziegler, L. D. *J. Chem. Phys.* **1990**, *92*, 2806.
(97) Kaweguchi, T.; Hijikigawa, M.; Hayafuji, Y.; Ikeda, M.; Fukishima, R.; Tomiie, Y. *Bull. Chem. Soc. Jpn.* **1973**, *46*, 53.
(98) Carter, C. F.; Levy, M. R.; Grice, R. *Faraday Discuss. Chem. Soc.* **1973**, *55*, 357. Logan, J. A.; Mims, C. A.; Stewart, G. W.; Ross, J. *J. Chem. Phys.* **1976**, *64*, 1804.
(99) Zhang, J.; Dulligan, M.; Segall, J.; Wen, Y.; Wittig, C. *J. Phys. Chem.* **1995**, *99*, 13680.
(100) Ree, J.; Kim, Y. H.; Shin, H. K. *Chem. Phys. Lett.* **1997**, *272*, 419.
(101) Janssen, M. H. M.; Dantus, M.; Guo, H.; Zewail, A. H. *Chem. Phys. Lett.* **1993**, *214*, 281. Guo, H.; Zewail, A. H. *Can. J. Chem.* **1994**, *72*, 947.
(102) Fotakis, C.; Donovan, R. J. *J. Chem. Soc., Faraday Trans.* 2 **1978**, *74*, 2099.
(103) Fan, Y. B.; Donaldson, D. J. *J. Phys. Chem.* **1992**, *96*, 19. Fan, Y. B.; Donaldson, D. J. *J. Chem. Phys.* **1992**, *97*, 189. Fan, Y. B.; Randall, K. L.; Donaldson, D. J. *J. Chem. Phys.* **1993**, *98*, 4700.
(104) Bodenstein, M. *Z. Phys. Chem.* **1894**, *13*, 56.
(105) Sapers, S. P.; Vaida, V.; Naaman, R. *J. Chem. Phys.* **1988**, *88*, 3638.
(106) Syage, J. A.; Steadman, J. *Chem. Phys. Lett.* **1990**, *166*, 159.
(107) Marvet, U.; Dantus, M. *Chem. Phys. Lett.* **1996**, *256*, 57.
(108) Young, M. A. *J. Phys. Chem.* **1994**, *98*, 7790. Young, M. A. *J. Chem. Phys.* **1995**, *102*, 7925.
(109) Randall, K. L.; Donaldson, D. J. *J. Phys. Chem.* **1995**, *99*, 6763.
(110) Cho, C.-C.; Polanyi, J. C.; Stanners, C. D. *J. Chem. Phys.* **1989**, *90*, 598.